

Landmark-based Vehicle Self-Localization Using Automotive Polarimetric Radars

Fabio Weishaupt , Julius F. Tilly , Nils Appenrodt , Pascal Fischer , Jürgen Dickmann 
and Dirk Heberling , *Senior Member, IEEE*

Abstract—Automotive self-localization is an essential task for any automated driving function. This means that the vehicle has to reliably know its position and orientation with an accuracy of a few centimeters and degrees, respectively. This paper presents a radar-based approach to self-localization, which exploits fully polarimetric scattering information for robust landmark detection. The proposed method requires no input from sensors other than radar during localization for a given map. By association of landmark observations with map landmarks, the vehicle’s position is inferred. Abstract point- and line-shaped landmarks allow for compact map sizes and, in combination with the factor graph formulation used, for an efficient implementation.

Evaluation of extensive real-world experiments in diverse environments shows a promising overall localization performance of 0.12 m RMS absolute trajectory and 0.43° RMS heading error by leveraging the polarimetric information. A comparison of the performance of different levels of polarimetric information proves the advantage in challenging scenarios.

Index Terms—Automotive radar, Millimeter wave radar, Radar polarimetry, Polarimetric radar, Localization, Radar signal processing

I. INTRODUCTION

WHILE for lower level advanced driver assistance systems radar sensors mainly focused on other road users, this is no longer sufficient for automated driving functions. One reason for this is the requirement that the vehicle must know its position and orientation (pose) very precisely and with high reliability, e.g. for path planning. The availability and precision of classical global navigation satellite systems (GNSS) are inadequate. Although differential GNSS approaches might meet the precision requirement, they are not available in scenarios without an unobstructed view to the satellites, e.g. in tunnels or between high-rise buildings. Therefore, exteroceptive sensors are used to perceive the static environment in order to derive pose estimates from that [1].

Manuscript received August 13, 2023; revised March 2, 2024. Date of publication ZZZ. This work results from the cooperative project @CITY – Automated Cars and Intelligent Traffic in the City – and is supported by the Federal Ministry for Economic Affairs and Energy on the basis of a decision by the German Bundestag. The Associate Editor for this paper was XXX. (*Corresponding author: Fabio Weishaupt.*)

Fabio Weishaupt, Nils Appenrodt, Julius F. Tilly and Jürgen Dickmann are with Research & Development at Mercedes-Benz AG, 70565 Stuttgart, Germany (e-mail: fabio.weishaupt@mercedes-benz.com).

Pascal Fischer was with Research & Development at Mercedes-Benz AG, 70565 Stuttgart, Germany.

Dirk Heberling is with the Institute of High Frequency Technology, RWTH Aachen University, 52074 Aachen, Germany, and with the Fraunhofer Institute for High Frequency Physics and Radar Techniques FHR, 53343 Wachtberg, Germany.

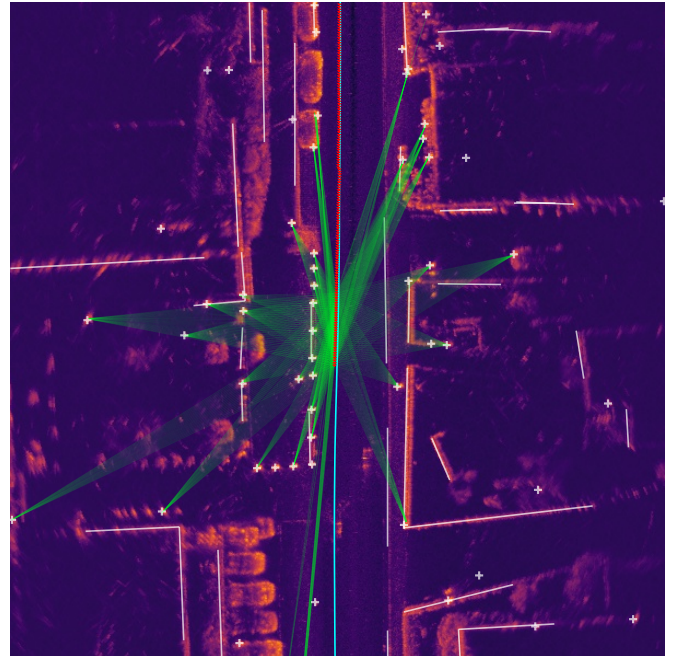


Fig. 1. The proposed localization framework estimates the ego-vehicle’s pose by optimizing a sliding window pose graph. An association (green) is shown for each pose from which a map landmark (white) is observed. The resulting localization trajectory is shown in red, the ground truth trajectory in cyan.

For robustness, multiple sensor modalities are typically combined, with one of them often being radar. While camera and lidar benefit from higher angular resolution, they suffer from a lack of direct range measuring capability and high cost, respectively. In contrast, radar has moderate costs and is a modality that has been integrated into serial products for decades. Furthermore, radar is robust to inclement weather conditions such as rain, fog and snow due to a comparatively long wavelength [2]. Even though first experimental frequency modulated continuous wave lidar prototypes are being built, radar is still the only serially produced long-range sensing modality capable of measuring relative velocity instantaneously. This is desirable for localization applications, as one can easily distinguish between other moving road users and the static environment [3].

In order to derive meaningful pose estimates from exteroceptive sensor data, a map containing a priori knowledge about objects expected in a given environment, including their positions, is required (cf. Fig. 1). If the map objects are georeferenced, a relative localization within this map corresponds to global localization. The representation of the map elements can vary considerably, ranging from a raw

collection of measurements from a previous mapping pass, over a grid-based representation, to landmarks. The memory size requirements decrease in the given order, so only the landmark-based approach is considered feasible for large-scale nationwide applications. Typical landmarks suitable for radar include point-shaped objects such as tree trunks, guideposts, traffic sign and street lamp poles, as well as line-shaped areas like curbstones, buildings and fences [4].

Polarimetric radar is an established technique in space- and airborne remote sensing applications for several decades [5]. By transmitting and receiving different polarizations, additional information about the scattering mechanisms that occurred during signal propagation can be derived. A classic example for airborne systems is the polarimetry-based distinction between single-bounce scattering of the sea and double-bounce scattering of buildings in urban environments. Although the measurement setup and operating frequency of airborne radars are significantly different from ground-based automotive applications, the fundamental principle of scattering parity can be transferred. Simple single-bounce objects such as poles of traffic signs or street lamps fall into the category of odd-bounce scattering, whereas door or window recesses of buildings and guardrail posts are typical examples of even-bounce scattering [6], [7], [8]. With the everlasting desire for an increasing number of channels in order to further improve angle finding in automotive radars, highly integrated circuits (ICs) became available in recent years such that three-digit channel counts can be realized by application of the multiple-input multiple-output (MIMO) principle in form factors that are feasible for passenger vehicle packaging. Therefore, the disadvantage of needing more channels for polarimetry is no longer prohibitive. While one has to accept some disadvantages in angle finding when available channels are spent for polarimetry, the number of remaining channels is still sufficient for an usable angle finding due to the initial large number with the latest ICs. Moreover, angular resolution and sidelobe levels, which would benefit from high channel counts, are typically not performance limiting factors for localization applications. Due to the assumption of a moving ego-vehicle, the static surroundings can be resolved by Doppler.

This publication proposes a complete landmark-based localization framework that exploits polarimetric information by identifying and localizing landmarks more reliably and precisely in comparison to non-polarimetric approaches. Based on the introduced polarimetric representation of the static environment, the capability to distinguish between different scattering mechanisms is used to improve the localization accuracy without the requirement to store polarimetric information in the map. By omitting the latter, the proposed approach does not depend by principle on a mapping vehicle with a polarimetric radar avoiding a potentially prohibitive disadvantage. The measurement setup used is fully polarimetric, i.e. the full complex scattering matrix is available. By selecting different subsets of the full matrix, the benefit of different polarimetric implementations of such a system can be compared, i.e. whether a dual-polarimetric system capable of discriminating between even- and odd-bounce scattering already provides the pursued key advantage.

The main contributions of this article are:

- Adaption of a radar-based ego-motion estimation approach to counteract a typical drawback of polarimetry,
- Scalable static environment representation created from low-level polarimetric data,
- Polarimetry-leveraging radar-only localization framework which is based on point- and line-shaped landmark maps,
- Evaluation of real-world localization performance using different levels of polarimetric information.

The paper is structured as follows. Section II provides a comprehensive review of literature related to finding the ego-vehicle's pose and related to polarimetric radar in automotive contexts. The proposed polarimetric, landmark-based localization approach is described in detail in Section III. Based on the description of the experimental vehicle setup and the evaluation framework, the results of the experiments are presented and discussed in Section IV. Finally, Section V concludes the article and gives an outlook on possible future research directions.

II. RELATED WORK

A sizeable body of literature exists on the vehicle self-localization using exteroceptive sensors. The majority of work is based on lidar or camera sensors with a recent increase in interest in using radar. Due to the radar focus of this work, the other sensor modalities are not covered in this section. For this, the reader is referred to a recent review paper [1]. The research area related to the estimation of the ego-vehicle's pose using radar sensors includes several sub-fields: simultaneous localization and mapping (SLAM), place recognition, ego-motion estimation and map-based self-localization.

SLAM is an approach to solve mapping and trajectory estimation in unknown environments at the same time. While such techniques are interesting for creating the a priori map for map-based self-localization, the achieved accuracies on longer routes and the loop closure requirement for improved accuracy [3], [9] renders SLAM insufficient as the sole source of pose information in automated driving applications. Although place recognition is also a technique for estimation of the ego-vehicle's location, it is not comparable to finding consistent sub-meter accurate trajectories because errors within a few meters are considered a successful localization [10], [11].

Therefore, SLAM and place recognition objectives are too different from this paper's focus such that only the literature on the two remaining sub-fields is considered in more detail in the following. Because polarimetry is still relatively unexplored in the automotive radar community, a short overview of the research directions is given and the preparatory work for this paper is presented.

A. Ego-motion estimation

Ego-motion estimation is a technique to derive the parameters of motion that the ego-vehicle is experiencing (usually translational and angular velocities). By integrating the estimates over time, an ego-pose can be calculated. However, the result will increasingly drift with longer integration times, so that using it alone is not sufficient for automated driving. Nevertheless,

ego-motion estimation is often part of a localization system where the drift error is corrected by map correlation. For radar-based ego-motion estimation, two different approaches are common, depending on the type of radar used. Mechanically scanning 360° radars, such as those used in the public “Oxford Radar RobotCar Dataset” [12] and “MulRan Dataset for Urban Place Recognition” [13] dataset, have no Doppler measurement capability, so two consecutive scans must be matched. This typically involves finding and matching keypoints between the scans and is still subject of research with both classical [14], [15] as well as learned approaches [16], [17]. For common automotive radars with a beamforming-based angular and Doppler-based velocity measuring capability, the motion state can be estimated instantaneously from a single scan by exploiting the dependence of the measured radial velocity on the azimuth angle for static infrastructure [18].



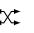

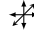
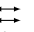




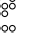



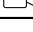
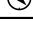
B. Radar-based self-localization with maps

This section provides an overview of work related to finding the ego-vehicle’s pose relative to an a priori map by using radar. Because the amount of research in this exact field is still limited, it is immature in a sense that no gold standard approach has been established yet. Therefore, this overview is broad and includes approaches that in part differ greatly. It is intended to help the reader put this work into context. Table II accompanies this section for a clear and concise comparison.

One of the most important differentiating factors between the approaches is the used sensor setup during the localization phase. The type of radar and any additional supportive sensor modality both play a crucial role for the system’s design. Table I introduces pictograms for brevity in Table II. Accordingly, each work is classified into one of the following three categories of radar: (*automotive*) *beamforming*, (*mechanically*) *scanning* or *ground penetrating radar*. The optional + symbol indicates that the used radar is polarimetric.

The former two scan the vehicle’s above-ground environment and are therefore suitable for advanced driver assistance system functions such as adaptive cruise control or blind spot monitoring in addition to localization. In contrast, ground penetrating radars only scan for sub-surface features and are limited to localization applications [22], [30]. The distinction between the two radar types (beamforming & mechanically scanning) perceiving the above-ground environment was already introduced in II-A. Further considerations for or against one of these radar types include the number of sensors needed for omni-directional coverage, ease of integration and packaging, vehicle design, power consumption, update rate and wear [38].

TABLE I
TRANSLATION OF SENSOR AND MAP TYPE SYMBOLS

Sensor Types		Map Types
 Beamforming radar	 Gyroscope	 cross-modal
 Scanning radar	 Accelerometer	 mono-modal
 Ground penetrating radar	 Speedometer	 sparse
+ Polarimetric radar	 Steering angle	 quasi-dense
 Lidar	 GNSS	 dense
 Camera	 Magnetometer	





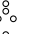

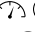



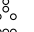

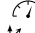


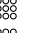

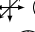


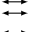
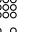

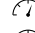


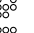



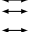


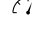


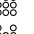


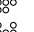

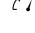


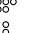







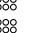

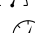



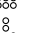

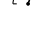





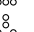


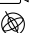


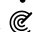



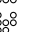


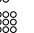




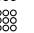

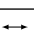
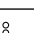

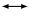
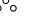
As far as the additional sensing modalities are concerned, most approaches rely on motion information from proprioceptive sources such as wheel tick and gyroscope sensors. These measurements typically serve as an initial pose estimate and are subsequently corrected for any drift by the exteroceptive sensor measurements. Only a minority of approaches is radar-only. They derive the odometry from the radar alone, either through scan matching [26], [32], [35], [37] or instantaneous Doppler-based estimation [28]. When different combinations of sensor modalities are evaluated in the paper, the minimal set that includes radar and the corresponding localization error is chosen for better comparability in Table II. Due to the different research directions of the considered papers, the route lengths for error evaluation differ considerably. However, in order to provide a comprehensive overview to the reader, the wide variety of approaches is still included. If different routes are used for evaluation or if multiple passes of the same route are evaluated, Table II lists the longest unique route.

Another distinctive property of each localization approach is the map type. The general categories for classification are: *sparse* versus *dense* and *cross-modal* versus *mono-modal* (for pictograms see Table I). The former differentiation describes the density of landmarks in the map and serves as an indicator for the required memory size to store the map and consequentially the scalability for large-scale deployments. Cross-modal maps are acquired with a sensor modality other than the one used during the localization phase, whereas mono-modal maps are usually constructed from measurements with the same sensor setup that is intended for localization.

Sparse, cross-modal map representations include manually surveyed positions of artificial beacons [19] as well as pole-like objects in semantic high definition (HD) maps [28], [31]. In contrast, sparse, mono-modal maps are the result of feature extraction algorithms applied to measurement data of the same sensors used during localization [20], [33]. The advantages of desirable scaling properties of sparse maps are accompanied by a more challenging association between online measurements and map elements as well as a higher probability of ambiguities when compared to dense maps. With regard to dense, mono-modal maps, the density covers a wide range, so that a further distinction between quasi-dense and dense is made in Table II. It ranges from a point cloud clustered over multiple measurement cycles [23], over a simple accumulation of unfiltered [29], [24] and filtered [35] point clouds as well as image-like two-dimensional grids [25], [34], [36], to volumetric grids for the ground penetrating systems [22], [30]. Large-scale deployments of ground penetrating localization are challenging not only due to the large memory footprint, but also because each lane of a road must be mapped individually. For all other approaches, a single pass is conceptually sufficient. The remaining dense, cross-modal approaches take advantage of better availability of camera- and lidar-based maps compared to radar. These range from map matching techniques based on density map correlation of visual SIFT features with radar detection density maps [27], over the transformation of radar images into lidar representations using a generative adversarial network [32], to end-to-end registration networks between radar and lidar images [37].

TABLE II

OVERVIEW OF APPROACHES TO MAP-BASED SELF-LOCALIZATION USING RADAR SENSORS. RESULTING LOCALIZATION ERRORS ARE GIVEN AS RMSE VALUES UNLESS OTHERWISE NOTED. THE SYMBOL \dagger INDICATES THAT 68 % OF ERRORS WERE BELOW THE GIVEN VALUE. THE SYMBOL * DENOTES MAE VALUES, # MARKS INDIRECT VALUES, E.G. ESTIMATES FROM GRAPHS.

Author	Reference	Year	Sensor Set		Route	Map		Error (m)	
			Radar	additional		Modality	Sparsity	longitudinal	lateral
Clark et al.	[19]	1998	1x 	 	0.2km			–	–
Lundgren et al.	[20]	2014	1x 	  	5 km			$\approx 0.50\#$	$\approx 0.50\#$
Rapp et al.	[21]	2015	4x 	 	0.1 km			$0.16\ddagger,\#$	
Cornick et al.	[22]	2016	1x 	  	1.6 km			0.06	0.04
Schuster et al.	[23]	2016	4x 	 	0.4 km			$> 1.0\#$	
Ward et al.	[24]	2016	2x 	 	5.4 km			0.38	0.07
Yoneda et al.	[25]	2018	9x 	 	2.2 km			0.19	0.26
Li et al.	[26]	2019	1x 	–	0.2 km				0.65
Iannucci et al.	[27]	2020	3x 	 	1.5 h			$\approx 0.3\ddagger,\#$	
Jürgens et al.	[28]	2020	6x 	–	2 km			$0.20\ddagger,\#$	$0.25\ddagger$
Narula et al.	[29]	2020	3x 	 	1.5 h			$\approx 0.3\ddagger,\#$	
Ort et al.	[30]	2020	1x 	  	7 km			0.17^*	0.26^*
Pishevvari et al.	[31]	2020	1x 	 	0.2 km				0.16
Yin et al.	[32]	2020	1x 	–	9 km				> 6.0
Engel et al.	[33]	2021	2x 	 	6 km			0.18	0.16
Otake	[34]	2021	5x 	 	1.4 km			0.07	0.07
Burnett et al.	[35]	2022	1x 	–	8 km			0.13	0.12
Yanase et al.	[36]	2022	9x 	 	4.6 km			0.16	0.14
Yin et al.	[37]	2022	1x 	–	9 km			≈ 1.0	
This work		2022	3x 	–	10 km			0.11	0.06

The reported error values are provided as root mean square errors (RMSE) in lateral and longitudinal directions, where available. These values serve as an indication of the order of magnitude rather than as a direct criterion for comparison, since the map and sensor qualities as well as the test environments differ significantly. Some work includes localization results in challenging environments such as snow. For better comparability, these values are not reported, but those of optimal results under regular conditions. If no separate evaluation of lateral and longitudinal directions is available, the joint error in the horizontal plane is given. When no RMSE values are available, it is denoted with \dagger and *. The former indicates the 68 % interval derived from a cumulative error distribution function (equivalent to RMSE if distribution is assumed zero mean Gaussian). The symbol * denotes the alternative error is calculated as the mean absolute error (MAE).

C. Polarimetric radar in automotive applications

While polarimetric radar for automotive applications is experiencing increasing interest in recent years, most of the literature deals either with the realization of such systems [39], [40] or with improved classification of road users [41], [42]. Recent publications on polarimetric synthetic aperture radar imaging [43], [44] are closer to localization and give a first impression of the potential benefits of polarimetry for landmark discrimination. Although this article’s authors are not aware of any recent publication on polarimetry-based localization, one of the early radar-based localization implementations relies heavily on polarimetry. In order to unambiguously identify manually placed beacons for localization, the beacons are

designed to show a unique polarimetric signature to the radar [19]. In their subsequent work, the radar’s polarimetric capability helps to recognize characteristic natural landmarks by their even bounce scattering response [45].

The authors of this publication have published several papers related to polarimetric localization. By demonstrating the highly anisotropic scattering behavior of typical objects in automotive environments, the need for special handling of polarimetric data in gridmaps to realize the full potential is proven [46]. To deal with the changing scattering mechanisms, an approach involving incorporation of detection-level data into a polarimetric covariance representation per grid cell is proposed [8]. Based on this, a landmark detector is developed that shows increasing robustness as the amount of polarimetric information increases [47]. In addition to the power comparison in conventional constant false alarm rate (CFAR) detectors, the proposed detector includes the polarimetric scattering difference in its decisions, which is why it is referred to as a polarimetric CFAR (pCFAR) in the following. Finally, a gridmap construction technique taking advantage of low-level data is introduced to represent the static environment as completely as possible, although still non-polarimetric [48]. The designation of low-level spectral data as PreCFAR data is introduced in this paper emphasizing the raw nature of this data level being tapped off before any detector stage.

This paper introduces the novel combination of low-level PreCFAR data and polarimetric covariance gridmaps bringing together the most complete environment representation with a sensible inclusion of polarimetric characteristics. Furthermore, this paper is the first to analyze the impact of different levels of polarimetric information on automotive localization accuracy.

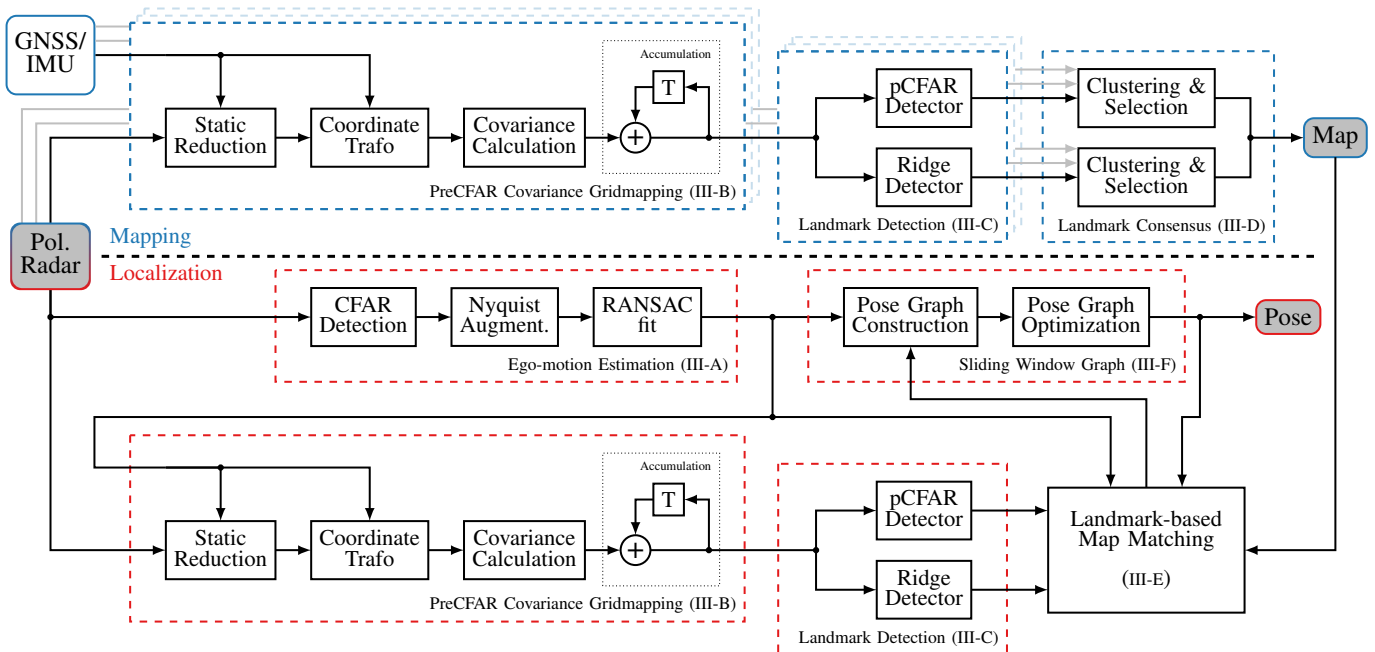


Fig. 2. The block diagram of the proposed approach contains the **mapping** (upper) as well as the **localization** part (lower). Lighter colored blocks and connections symbolize the multiple drives through the same environment for map creation, which are merged in the last mapping step.

III. PROPOSED APPROACH

In this section, the proposed self-localization approach is described in detail. It is based on point- and line-shaped landmarks such that the corresponding maps are compact, which is necessary for a scalable approach as mentioned above. The main challenge to overcome for achieving a precise and reliable localization is a robust and repeatable landmark detection. Only then can the right association of observed landmark candidates with map landmarks be made. For this, an accumulation of multiple frames is necessary in radar applications because otherwise a lot of false positive point-shaped landmark candidates would be extracted due to noise and only partial line-shaped landmarks could be identified due to the single observation point. Furthermore, the robustness shall be improved by leveraging polarimetric information. The proposed implementation is developed to fulfill the combination of these requirements and all the necessary building blocks are discussed in the following subsections. The block diagram in Fig. 2 gives an overview of the parts involved.

A. Ego-motion Estimation

The instantaneous estimation of the ego-vehicle's motion state based on Doppler radars is well-known for automotive applications. The static environment is observed by the radar sensors with a relative velocity that is of the same magnitude as the vehicle's velocity, but with an opposite sign. Because the sensors measure only the radial component of the velocity, a sinusoidal dependence over the observation angle is expected. By estimating the sinusoid's parameters and combining them with the mounting pose of the sensor, one can infer the motion state. For this, reflections from the static surroundings need to be distinguished from other dynamic traffic participants. A random sample consensus (RANSAC) technique is suitable for this [18]. It is the basis of the ego-motion estimation

in this work. A motion state with two degrees of freedom $\mathbf{m}_{\text{ego}} = (v_{\text{ego}}, \omega_{\text{ego}})$ referenced to the vehicle's rear-axle center including a forward velocity and yaw rate is considered sufficient (zero-side-slip assumption). Any errors due to a violation of this assumption are considered small enough that the subsequent localization can handle and compensate those. Limiting accelerations to a range of physically reasonable values allows rejecting outliers that may occur when the static environment is not the origin of the majority of detections, e.g. in dense traffic. Because the algorithm is sensitive to mounting pose errors, the calibration has to be carried out carefully. Alignment between the polarimetric channels is one of the peculiarities that have to be taken into account. However, due to this work's focus, the reader is referred to [49] for details.

Compared to the original work [18], some additional steps help to improve accuracy and robustness in a real-world application. For non-negligible accelerations, motion estimation including multiple sensors can suffer from synchronization errors due to a sequential triggering for interference avoidance. Extrapolation of motion information from previous estimates is used to minimize this effect [28]. Thereby, the respective last measurements of each sensor can be included in a combined estimation for more robust and precise results.

Furthermore, additional attention is needed for ego-velocities outside of the unambiguous Doppler range. In order to measure the different components of the scattering matrix, fully polarimetric implementations typically switch between polarizations in a time multiplex scheme, which can result in small unambiguous Doppler velocities (cf. Table III). A straightforward implementation might involve carrying out all calculations in the 0th Nyquist zone, i.e. the domain in which all measured velocities including potentially aliased ones are located. However, this would require a repeated folding of the fit function and usage of cyclic distances for inlier calculation. This is why an alternative augmentation

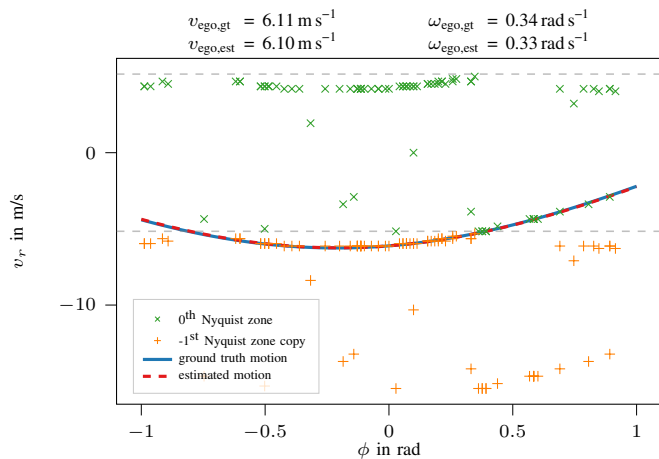


Fig. 3. By the proposed Nyquist zone augmentation, the ego-motion estimation also provides correct results beyond the unambiguous Doppler velocity.

approach is pursued in this work, which might be more efficient even though the number of detections is multiplied. Depending on the expected range of ego-velocities and the unambiguous Doppler velocity, a number of Nyquist zones is determined that shall be covered. Then, each detection is copied to the corresponding positions in all zones such that the regular RANSAC algorithm without model function folding and cyclic distance calculation can be applied. Due to the algorithm’s objective to identify the largest group of consistent velocities, the introduced invalid samples are not misleading the estimation result. This approach of simple but highly parallelizable operations is particularly suitable for modern, parallel computing architectures. A simplified example (only one copy for clarity) is shown in Fig. 3, where the ego-velocity is slightly above the unambiguous Doppler velocity for a single front-mounted sensor such that the samples in broadside direction are aliased into the 0th Nyquist zone. Due to the proposed Nyquist zone augmentation, the RANSAC algorithm is still able to produce a valid estimate that is very close to ground truth.

B. PreCFAR Covariance Gridmaps

The proposed localization framework builds around a specifically engineered representation of the static environment. This article’s authors have addressed some challenges involved with using polarimetric radar for self-localization in a series of preceding work. While the core concepts and their motivation for PreCFAR gridmaps on the one hand and the covariance representation on the other hand are given in Sections III-B1 and III-B2, references to the corresponding publications will help the reader to study the details. Finally, the novel integration of both previous concepts is proposed in Section III-B3.

1) *PreCFAR Gridmaps*: For a rich representation of the surroundings that allows extracting potential landmarks in a robust way, the accumulation of multiple measurement cycles is a well-known technique. To account for the motion of the ego-vehicle, this accumulation is typically carried out in a world-fixed coordinate system in the form of gridmaps. In radar applications, the estimated quantity per grid cell could be occupancy or reflectivity [50]. Historically, the radar

measurements for incorporation into the gridmap were in a sparse detection list format as a result of CFAR filtering. This leads to an incomplete mapping in case of low-reflectivity or extended objects because of a low probability of detection and the CFAR’s inherent masking property. Therefore, a technique to counteract this is based on the use of lower-level data that has not passed a CFAR filtering stage [48]. For using this data level, either a sensor with a higher processing power than is usual today needs to carry out the whole gridmap computation, or a higher bandwidth interface has to be used that is able to transfer the increased data rates. The latter is becoming possible soon with Ethernet becoming the common standard interface to the radar and emerging compressed representations of low-level data. An additional advantage of the more centralized architecture is the option to perform low-level multi-sensor fusion.

Starting from a processed radar data cube, the static surroundings are located on a sinusoidal shaped surface as depicted in Fig. 4. The ego-motion leads to the same dependency of the measured Doppler velocity on the azimuth angle as described in Section III-A, regardless of the range. Applying the Fourier modulation theorem in an appropriate way [48], this surface is extracted from the data cube and a dense image-like representation of the static environment in polar coordinates is obtained (“Static reduction” in Fig. 2). For performing the accumulation of multiple measurements spatially correct, a transformation to Cartesian coordinates is carried out via nearest neighbor interpolation. Both steps require ego-motion information. Linear and angular velocities determine the position of the surface in the data cube, whereas a pose defines the parameters for the coordinate transformation. In case of the mapping phase, ground truth motion data can be used. During the localization phase, the trajectory within a sliding window needs to be smooth and must not negatively influence the accumulation by localization errors. For this reason, the integral of the estimated ego-motion is used instead of the localization result (cf. Fig. 2, there is no feedback loop of the pose result). The sliding window size is limited by the drift introduced by the imperfect estimates. The maximum acceptable drift needs to be derived from the subsequent module and should be of the same order of magnitude as the grid’s cell size in this case.

2) *Polarimetry & Covariance Gridmaps*: While conventional automotive radars measure a scalar reflectivity, usually expressed as a radar cross section (RCS), a polarimetric radar estimates multiple reflectivities for each cell in the data cube. Because a fully polarized electromagnetic wave can be represented by a superposition of two orthogonal basis polarizations, a scattering event can be fully characterized by a 2×2 matrix, assuming narrow-band and far-field conditions. This can be interpreted as two separate responses of the scattering object for each of the two incident polarizations and consequently for any superposition due to linearity.

Although the transmitting and receiving polarization bases may not be the same in general, only one basis \mathcal{B} is assumed for both in the following. In case of a fully polarimetric measurement, this is possible without loss of generality because a purely mathematical transformation to any basis is feasible.

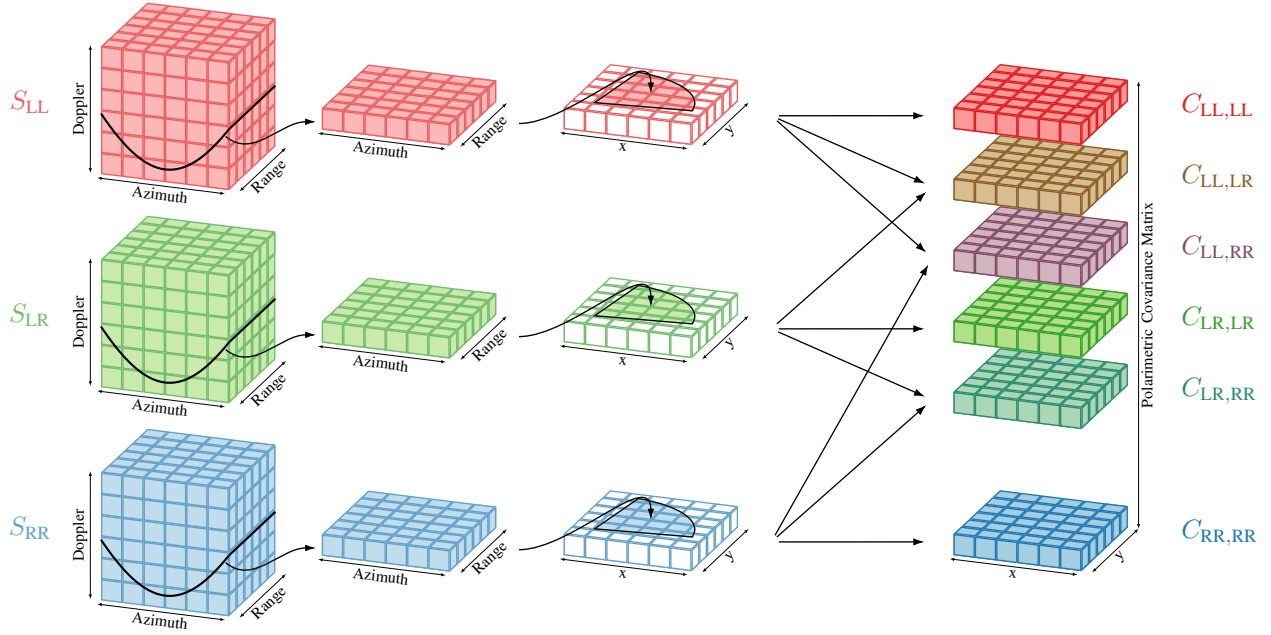


Fig. 4. PreCFAR covariance gridmaps combine a low-level radar data utilization with a meaningful accumulation of polarimetric information for incorporation into a gridmap. As a result, the superposition of scattering mechanisms and extended objects are well represented.

Then, the elements $S_{ab} \in \mathbb{C}$ with $a, b \in \{L, R\}$ constitute the complex scattering matrix $\mathbf{S}_{\mathcal{B}_{LR}}$ in a circular basis \mathcal{B}_{LR} with a sent polarization b , received polarization a and L, R for left- and right-hand circular polarization, respectively. Unless otherwise noted, a circular polarization basis \mathcal{B}_{LR} is chosen implicitly and all polarimetric quantities are given with reference to this basis ($\mathbf{S} = \mathbf{S}_{\mathcal{B}_{LR}}$). In the following, the vectorized representation of the scattering matrix

$$\boldsymbol{\Omega} = \text{vec}(\mathbf{S}) = (S_{LL} \ S_{LR} \ S_{RL} \ S_{RR})^T \quad (1)$$

will be used with $\boldsymbol{\Omega} \in \mathbb{C}^q$. The dimensionality q indicates if fully polarimetric data is used ($q \in \{3, 4\}$), a dual polarimetric configuration is evaluated ($q = 2$) or a non/single polarimetric experiment is carried out ($q = 1$). A scattering vector of length $q = 3$ still has full polarimetric information in case of a monostatic radar setup and reciprocal propagation media because both originally anti-diagonal terms are identical ($S_{LR} = S_{RL}$). In the non-polarimetric case, the only remaining absolute phase provides no usable information and could be neglected ($q = 1 \rightarrow \boldsymbol{\Omega} \in \mathbb{R}$). Due to the used covariance formulation that is introduced below, this happens inherently by the covariance definition. In a circular basis, S_{LL} and S_{RR} correspond to even-bounce scattering, S_{LR} and S_{RL} to odd-bounce scattering.

While the scattering vector can properly describe the observation of a single scattering event, it is an inappropriate representation for a superposition of multiple scattering observations in a single gridmap cell. Such a superposition can occur for various reasons: on the one hand, multiple objects with different polarimetric signatures could be located in the same grid cell; on the other, an anisotropic object that is observed from diverse aspect angles either by multiple radars with different mounting positions or over time due to the ego-vehicle's motion [46]. A more suitable representation is found by modeling the scattering information as a stochastic

process via its second order moment [8]. Therefore, a sample covariance matrix \mathbf{C} over a sample size of $N \in \mathbb{N}$ is calculated per grid cell by averaging the outer products of the corresponding scattering vectors $\boldsymbol{\Omega}_k$ over time and different sensors as

$$\mathbf{C} = \frac{1}{N} \sum_{k=1}^N \boldsymbol{\Omega}_k \boldsymbol{\Omega}_k^H \quad (2)$$

with $\mathbf{C} \in \mathbb{C}^{q \times q}$ and superscript H as the Hermitian transpose.

3) *PreCFAR Covariance Gridmaps*: The combination of both previously introduced concepts is novel and builds the basis for the localization. As depicted in Fig. 4, the different polarization channels are processed separately with the proposed PreCFAR gridmapping technique first. At this point, one could comprehend the deliberate choice of a simple nearest neighbor interpolation: it prevents the introduction of distorted scattering responses that were never measured, but are purely a result of interpolation. For reasons of efficiency, the covariance calculation is performed *after* Cartesian PreCFAR gridmaps are created per polarization channel. Due to the Hermitian property of the covariance matrix, it is sufficient to compute and store only the diagonal and the upper off-diagonal elements. Instead of q^2 layers, the memory requirement is reduced to $\frac{q(q+1)}{2}$ layers for the compressed covariance format.

This processing block is used in both the mapping as well as in the localization phase (cf. Fig. 2). The only difference between both instances is the persistence of old measurement data. While during mapping it is assumed that the ground truth pose does not suffer from any drift, this is not valid for the integrated ego-motion estimation. Therefore, for mapping, the full history of each cell is used, which includes visits to the same area with different driving directions. For localization, on the other hand, the finite sliding window described in Section III-B1 is required to prevent smearing.

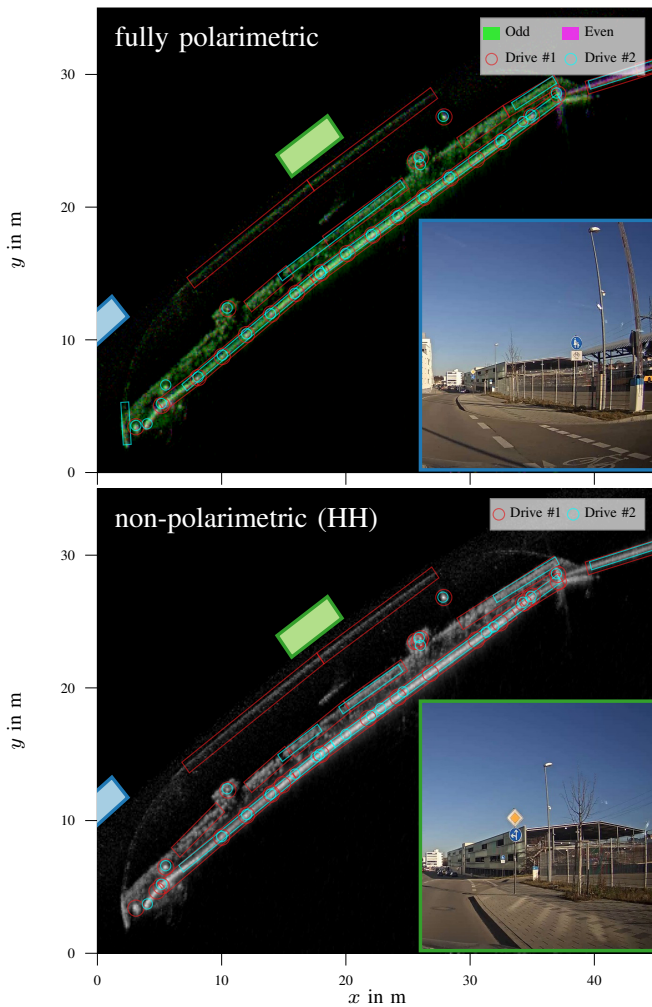


Fig. 5. The point- and line-shaped landmark candidates of the proposed extractors are shown for two drives in the same environment with an underlying PreCFAR gridmap of one of the drives. Comparing the non-polarimetric with the fully polarimetric experiment, the improved robustness of the point-shaped landmarks can be observed for the latter. The blue and green rectangles show the ego-vehicle positions where the optical images were taken.

C. Landmark extraction

The landmark-based localization relies on point- and line-shaped landmarks. Similar to the PreCFAR covariance gridmapping blocks, the same landmark detectors are used for both mapping as well as localization. Their working principles are detailed in the following.

1) *Point-shaped Landmarks*: For the detection of point-shaped landmarks, the polarimetric information of the covariance gridmap is exploited. This is motivated by the fact that an additional distinct scattering information helps detecting a landmark more robustly compared to the classical criterion of a characteristic amplitude. Evidence for this is demonstrated in [47] based on CFAR gridmaps of real-world measurements. The more polarimetric information was available to the detector, the better was the robustness of the extracted landmarks in terms of re-observability in multiple drives. This principle is transferred and newly applied to PreCFAR gridmaps in this paper and an example is given by Fig. 5. Using the amplitude as the sole quantity to extract characteristic areas in

the non-polarimetric case, only a few fence posts are detected. Additionally, the result is unstable as the intersection of locally corresponding landmarks is small for multiple visits of the same area. As the reflectivities of the fence elements and the posts are roughly similar, the extraction algorithm has no chance to generate robust results. The opposite is true if the characterization of the scattering mechanism by polarimetry is included. On a closer look, the posts show additional even-bounce scattering behavior such that a suitable algorithm is capable to robustly identify them as landmarks.

The underlying principle is based on a rigorous continuation of a probabilistic modeling of the polarimetric scattering vector. Starting from a multivariate complex Gaussian distribution with zero mean for the scattering vector Ω , a complex Wishart distribution can be derived as the probability density of the covariance matrix \mathbf{C} [51]. Combining this with Bayesian maximum likelihood classification theory, a simple distance measure

$$d_{\text{wishart}} = q^{-1} (\ln |\Sigma| + \text{tr} (\Sigma^{-1} \mathbf{C})) \quad (3)$$

allows one to compare the similarity of polarimetric covariance matrices with $|\mathbf{X}|$ and $\text{tr}(\mathbf{X})$ symbolizing the determinant and trace of matrix \mathbf{X} , respectively [47]. For landmark detection, this is applied in a similar fashion to cell averaging CFAR by comparing the covariance of the cell under test \mathbf{C} with a neighborhood average Σ , referred to as pCFAR. A threshold binarizes the resulting distance image and the centroids of connected areas are considered potential landmarks. For details, the reader is referred to [47].

2) *Line-shaped Landmarks*: For line-shaped landmark extraction, no polarimetric information is used because environments in which a significant benefit can be expected typically do not occur (extended object within another extended object similar in amplitude but different in scattering). Instead, the trace of the covariance matrix as a scalar measure of reflection power is the input to the algorithm. The first operation on this map is median filtering to reduce noise while preserving structure. Then, ridge detection is carried out using the eigenvalues of the Hessian matrix. The computed ridgeness score is thresholded and the result is skeletonized. Finally, a Hough transform extracts line segment candidates. Comparing the line-shaped landmark candidates in Fig. 5, no general difference is observed between the different levels of polarimetric information utilization. This is partly expected as no additional scattering information is used. Furthermore, it shows that the lowered power in the non-polarimetric case constructed by omitting some channels is not the limiting factor in this scenario.

D. Landmark Consensus & Map Construction

For map construction, the area of interest is passed multiple times with a known ground truth pose from a coupled system consisting of an inertial measurement unit (IMU) and a differential GNSS receiver. Hence, map construction in this work only considers scenarios in which the outage of satellite signal reception is limited to short time periods. Ground truth poses are also necessary to evaluate the localization accuracy.

However, that does not compromise the proposed localization approach itself, which would be most valuable in GNSS denied scenarios. It would just require other mapping methods mapping, e.g. incorporating SLAM or alternative ground truth positioning solutions, which is beyond the scope of this paper.

The stacked copies of the processing blocks in the lighter blue color in the mapping path of Fig. 2 symbolize the multiple drives for which a consensus has to be found. The rationale behind finding landmarks as an agreement over multiple drives is motivated by the assumption that a landmark is robust in the sense of easy recognition if it is seen multiple times. At the same time, this includes the removal of only temporarily stationary objects, such as parked cars or trash bins, which are not suitable as map landmarks.

For point-shaped landmarks, this is achieved by evaluation of the Euclidean distances between landmark candidate positions of the different passes. The landmark candidate positions of each combination of passes are queried for spatially close pairs via an efficient k -d tree data structure [52]. By interpreting the landmarks as nodes and the aforementioned closeness below a threshold $d_{lp,thres}$ as edges in a graph, a connected component algorithm is used to establish a landmark from a group of landmark candidates if a minimum number of observations $N_{lp,thres}$ is exceeded. The final landmark position is simply the average position of all group members.

Finding line-shaped landmarks is conceptually similar to the connected component merging of re-observed candidates with the difference of the distance measure. Instead of the Euclidean distance a combination of convex hull and projection distance is deployed and proximity is assumed when the corresponding values fall below the thresholds $d_{l, ch, thres}$ and $d_{l, prj, thres}$ [53]. Identified matching groups of candidates are merged as a line segment with the longest distance between all mutual projection points (cf. [53]). In case a series of line segments describing a curve form a group, shortcuts have to be prevented. Therefore, additional points are inserted in a similar fashion to the Ramer-Douglas-Peucker algorithm [54] until an upper error threshold is met. Lastly, if the line segments' ends cross or are just short of crossing, they are shortened or lengthened to the intersection point for a more compact representation in the map.

E. Landmark-based Map Matching

The robustness of the whole localization framework depends strongly on the map matching module. It has to unambiguously associate the potential landmark observations with actual landmarks in the map. The challenges to be overcome include finding the correct associations even in the case of partial overlap between both sets, and avoiding getting stuck in a local minimum, as observed in some common registration algorithms. Because this task is to some extent independent of the sensor modality used, there is a wider range of literature available. This allowed the adoption of many ideas from the initially modality-independent work [55] on a robust map-based self-localization framework. The evaluation of the framework is based on camera and lidar data in this publication, but an application of this to radar is also published [28].

First, landmark observations are collected in a local map frame that is purely based on the integration of ego-motion estimates (i.e. not result of the full localization to avoid self-reinforcing divergence). Therein, observations within a temporal window belonging to the same landmark are grouped according to their mutual distances. In contrast to [55], the clusters are calculated by finding connected components in a distance-weighted sparse graph derived from a k -d tree representation. This allows larger time windows for local map construction, because more drift is tolerable due to the connected component clustering. In general, the local map clustering enables correct association in case of a temporarily low number of landmarks observations.

Next, the local landmark clusters obtained in this way are matched with the map landmarks analogously to [55]. Both, point- and line-shaped landmarks contribute to the cost of a transformation candidate. As introduced in Section III-D, the Euclidean distance specifies the cost of point-shaped landmarks, whereas the sum of convex hull and projection distance is used for line-shaped landmarks. To avoid low cost but also low count matches, an additional cost is introduced for unmatched landmarks.

Finally, the temporal smoothing is again conceptually very similar to [55] by generally searching for the map landmark that was most often associated with a landmark observation. This filters out outlier matches. Note that this allows a map landmark to be associated with multiple observations. Therefore, the proposed implementation differs by aiming at an injective mapping between the observations and map landmarks. If there is a landmark observation without a correct counterpart in the map, and it is wrongly associated a few times to some map element, which actually corresponds to another landmark observation with a higher number of associations, both associations would outlast the temporal smoothing in the original formulation. Instead, the desired result is a maximum weight matching of a bipartite graph constructed from the corresponding association counts. Then, no map landmark will be associated with multiple observations after the temporal smoothing operation.

Based on the results of the described map matching approach, an association graph can be drawn for visualization. Poses $\mathbf{x}_x \in \text{SE}(2)$ ($x \in \{0, \dots, X-1\}$) are connected by the integrated odometry in their temporal order. If the result of the map matching is that a landmark \mathbf{l}_l ($l \in \{0, \dots, L-1\}$) is associated with an observation in some measurement cycle, the corresponding pose is connected to the landmark. Point-shaped landmarks are denoted with $\mathbf{l}_l^p \in \mathbb{R}^2$ and line-shaped landmarks with $\mathbf{l}_l^l \in \mathbb{R}^4$. A simple example of such an association graph is shown in Fig. 6.

F. Sliding Window Pose Graph Optimization

The pose estimate of the proposed approach is derived within a factor graph optimization framework. Again, this subsection is inspired by publication [55]. However, the graph formulation is an established technique and the cited reference is one of many. Furthermore, the handling of line-shaped landmarks is different from that in the cited publication and therefore the proposed approach is discussed in more detail below.

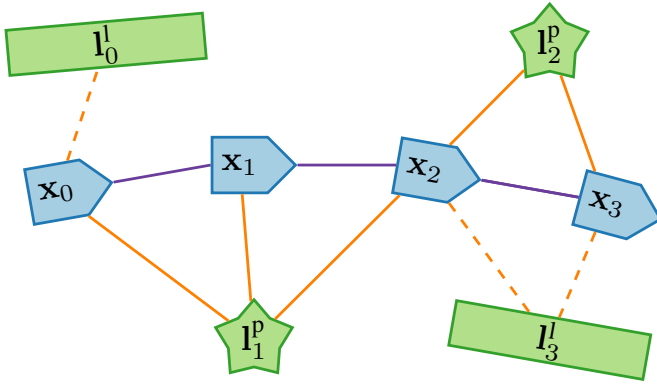


Fig. 6. The result of the map matching module is an association graph that connects point- (—) and line-shaped (---) landmark candidate observations with their corresponding map landmarks. Based on this, the pose graph is constructed for the subsequent optimization step (cf. Fig. 7).

Several properties make graph-based approaches advantageous for automotive self-localization: they have deterministic behavior and are able to integrate time-delayed information after ambiguity resolution. Although the intended application is localization, the landmark positions are still part of the estimation result in addition to the poses. This allows updating the map, but is beyond the scope of this work. The size of the factor graph is kept fixed at a certain duration in form of a sliding window. Due to the localization focus, outdated nodes are removed from the graph by truncation instead of marginalization to avoid fill-in [55]. According to this, the state to optimize $\Theta = (\mathbf{x}^T \mathbf{I}^T)^T$ consists of X poses $\mathbf{x} = (\mathbf{x}_0^T \cdots \mathbf{x}_{X-1}^T)^T$ and L landmarks $\mathbf{l} = (\mathbf{l}_0^T \cdots \mathbf{l}_{L-1}^T)^T$. These correspond to the variable nodes in the factor graph representation (cf. Fig. 7). The objective of the optimization is to find the state $\hat{\Theta}$ that is most probable given the measurements \mathbf{z} in a maximum a posteriori sense as

$$\hat{\Theta} = \underset{\Theta}{\operatorname{argmax}} p(\Theta | \mathbf{z}). \quad (4)$$

Applying Bayes theorem and assuming independent and identically distributed Gaussian densities for the measurements and priors, the optimization can be reformulated in form of a minimization as

$$\hat{\Theta} = \underset{\Theta}{\operatorname{argmin}} \sum_k e_k(\Theta, \mathbf{z}_k)^T \mathbf{P}_k e_k(\Theta, \mathbf{z}_k) \quad (5)$$

with the error function e_k and information matrix \mathbf{P}_k as the inverse of the covariance matrix corresponding to measurement \mathbf{z}_k . Factor nodes \mathbf{f}_k in a factor graph comprise the error function e_k , information matrix \mathbf{P}_k as well as the measurement \mathbf{z}_k and are the other part in the factor graph representation (cf. Fig. 7). While the index k in this summation stands for any existing factor to be considered, the nomenclature for a specific factor is as follows. If a factor is directly influencing only one variable, this *unary* factor \mathbf{f}_i^u is in relation with the variable node of type $u \in \{\mathbf{x}, \mathbf{l}^p, \mathbf{l}^l\}$ at index i . Analogously, for a *binary* factor $\mathbf{f}_{i,j}^{u,v}$ an additional variable node of type $v \in \{\mathbf{x}, \mathbf{l}^p, \mathbf{l}^l\}$ at index j is directly influenced. One can imagine them as containing a relative measurement between the involved nodes. Thus, four factor types are relevant for the localization task being

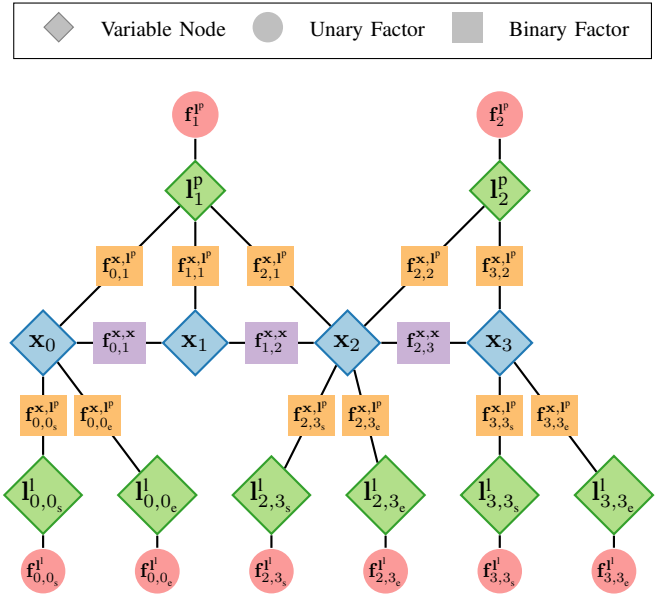


Fig. 7. The pose graph consists of nodes whose values are to be optimized, and factors that constrain the optimization. The ego-vehicle poses \mathbf{x} are the main nodes to be optimized whereas optimized landmark nodes \mathbf{l} are of more interest for map updates and less for the localization itself. This example is the equivalent pose graph to the association graph of Fig. 6.

- $\mathbf{f}^{\mathbf{x},\mathbf{x}}$: binary odometry factor,
- $\mathbf{f}^{\mathbf{x},\mathbf{l}^p}$: binary landmark observation factor,
- $\mathbf{f}^{\mathbf{l}^p}$: unary point-shaped map landmark prior factor,
- $\mathbf{f}^{\mathbf{l}^l}$: unary line-shaped map landmark prior factor.

Translation from the association result in Fig. 6 to a factor graph representation is shown in Fig. 7. The radar-based ego-motion estimate constrains successive pose variables. Forward and rotational velocities are integrated by an ordinary linear model to a position and heading delta, which serves as the factor's measurement $\mathbf{z}^{\mathbf{x},\mathbf{x}}$. For simplicity, the corresponding information matrices $\mathbf{P}^{\mathbf{x},\mathbf{x}}$ are chosen to be constant, and the error function is typically implemented in any graph optimization library via Lie group calculus.

Landmark observation measurements $\mathbf{z}^{\mathbf{x},\mathbf{l}^p}$ and their corresponding information matrices $\mathbf{P}^{\mathbf{x},\mathbf{l}^p}$ are often considered in polar coordinates to account for the sensor's uncertainties in the coordinate system that relates to its measurement principle. Again, the information matrices for all factors are constant in the polar coordinate system, and derivation is based on the sensor's accuracy and precision. Aspect angle dependencies are neglected. These binary factors are used for both point- as well as line-shaped landmarks with the latter being split into start and end point as described in the following.

Associated point-shaped map landmark positions constrain the landmark state with the global map position, which is introduced in form of a measurement $\mathbf{z}^{\mathbf{l}^p}$ within an unary factor $\mathbf{f}^{\mathbf{l}^p}$. For these factors, the Euclidean distance serves as the error function and a constant information matrix $\mathbf{P}^{\mathbf{l}^p}$ over all point-shaped map factors represents the map's uncertainty.

Line-shaped landmarks $\mathbf{l}^l = \left((\mathbf{l}_s^T) \quad (\mathbf{l}_e^T) \right)^T$ with $\mathbf{l}_s, \mathbf{l}_e \in \mathbb{R}^2$ and with the subscripts s and e denoting the start and end point of the line segment are handled as two point-shaped landmarks with tailored information matrices.

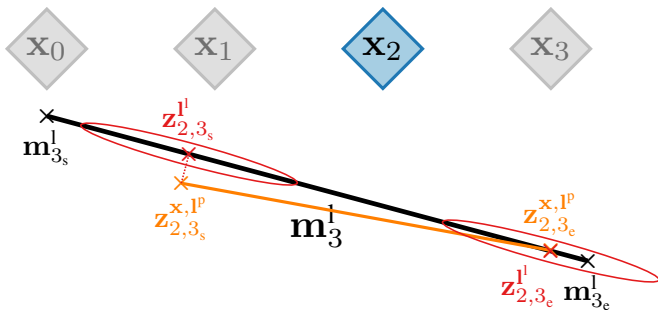


Fig. 8. The implementation of line-shaped landmark constraints is done by introducing two point-shaped landmark factors at the orthogonal projection points of the observation's start and end point onto the map landmark. The corresponding information matrices ensure that line-shaped landmark factors constrain mainly in a direction orthogonal to the map landmark's orientation.

For the line-shaped landmark l_3^l in Fig. 6, the observations per time instance are split into two point observations each in the pose graph in Fig. 7. Extra nodes for observation from pose x_2 and pose x_3 are inserted because different segments of the line landmark may be observed at different instances of time, e.g. due to occlusion. Fig. 8 illustrates how the map constraints are introduced for observation from pose x_2 . The start and end point of the observation are handled by two independent factors that are equivalent to the point-shaped landmark factors. Hence, the measurements are $z_{2,3_s}^{l,1^p}$ and $z_{2,3_e}^{l,1^p}$. Because the previous association step will only deliver a positive result when the match is rather good, it is reasonable to introduce the map constraints as the orthogonal projections onto the line landmark. The particularity is that the information matrices are chosen in a way that respects the line segments nature by strongly penalizing errors in the orthogonal direction compared to parallel (cf. Fig. 8). To indicate this, the map constraint factors f^l are having the line landmark superscript even though the variable nodes of start and end point have point landmark dimensionality. In order to distinguish between the start and end point of a line-shaped map landmark and the constraints for a specific observation, the former are denoted by m^l as opposed to the notation of measurements z corresponding to the factors in Fig. 8.

IV. EXPERIMENTAL EVALUATION

A. Experimental Vehicle Setup

The three polarimetric radar sensors are mounted in the experimental vehicle's front. An illustration of the measurement setup as well as photographs of the vehicle and sensor are depicted in Fig. 9. The radar parameters are listed in Table III. The dual circularly polarized transmit and receive antennas are implemented as corrugated horn antennas with septum polarizers in a waveguide front-end. Fully polarimetric information is acquired by concurrently receiving left and right hand circular polarization and switching the transmitter between left and right hand polarization sequentially as in time division multiplexing (TDM). This requires a compensation of the phases of the two halves of the scattering matrix. Otherwise, the perceived polarimetric information of the same scattering mechanism would depend on the relative velocity between the radar and the object. A compensation approach has been

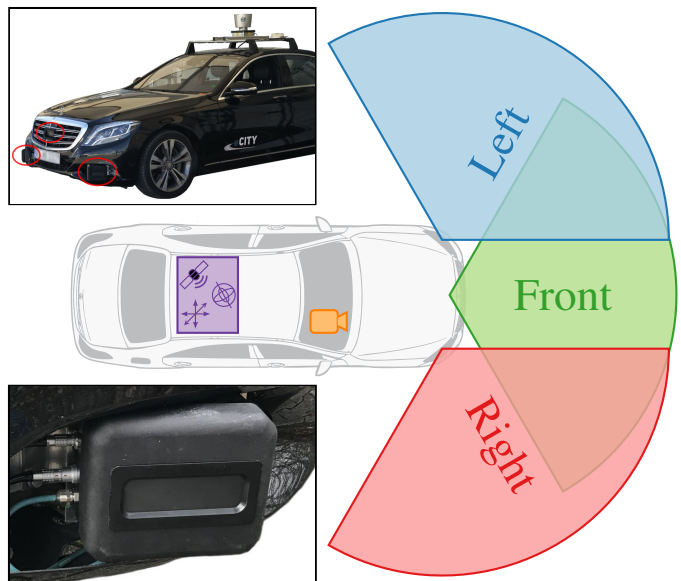


Fig. 9. The experimental vehicle is equipped with three polarimetric radar prototypes mounted in the front, a camera for documentation purposes and an integrated GNSS/IMU device for map creation and localization evaluation. No sensor other than radar is required for a localization pass, if no evaluation comparing to a ground truth is carried out, which is why the proposed approach is considered to be radar-only during localization. (upper left image: original photograph is property of @CITY consortium)

validated in [49]. Additional multiplexing in time domain is employed to extend the virtual array by a MIMO processing scheme. As a result, the unambiguous Doppler velocity is comparatively low. After demultiplexing, all four polarimetric channels are available at each virtual array position [49]. The raw analog-to-digital converter samples are available per Ethernet and allow processing the proposed PreCFAR gridmaps.

Furthermore, a camera is included for documentation purposes. For map construction and localization evaluation only, a coupled GNSS/IMU system is installed (Genesys Automotive Dynamic Motion Analyzer G PRO). Its data is not used in the localization pass itself. Post-processing improves the accuracy of the pose information by forward-backward smoothing. For evaluation of the localization, it is differentiated between a full-precision differential carrier phase solution and lower quality solutions. The device reports expected position errors in form of standard deviations from its internal Kalman filter. Based on this, the mean position standard deviation in the horizontal plane over all evaluated measurements is 14 mm for carrier phase solutions and 86 mm for the rest.

TABLE III
PARAMETERS OF THE USED POLARIMETRIC RADAR SENSORS.
RESOLUTION VALUES ARE BASED ON THE RAYLEIGH CRITERION.

Parameter	Value	Parameter	Value
Center Frequency	78 GHz	Azimuthal Field of View	$\pm 60^\circ$
Maximum Range	80 m	Azimuthal Resolution	$\sim 3^\circ$
Bandwidth	2 GHz	Unique Virtual Elements	31
Range Resolution	7.5 cm	Unambiguous Rad. Vel.	$\pm 5 \text{ m s}^{-1}$
Update Rate	10 Hz	Rad. Vel. Resolution	0.15 m s^{-1}
Polarimetric MIMO	TDM	Polarization Basis	LR

TABLE IV
INFORMATION MATRIX PARAMETERS

Information Matrix	Parameter
$\mathbf{P}^{\text{lp}} = \text{diag}(\sigma_{\text{lp}}^2, \sigma_{\text{lp}}^2)^{-1}$	$\sigma_{\text{lp}} = 0.1 \text{ m}$
$\mathbf{P}^{\text{l}} = \left(\mathbf{U} \text{diag} \left((10\sigma_{\text{l}})^2, \sigma_{\text{l}}^2 \right) \mathbf{U}^T \right)^{-1}$	$\sigma_{\text{l}} = 0.1 \text{ m}$ \mathbf{U} rotation acc. to Fig. 8
$\mathbf{P}^{\mathbf{x}, \mathbf{x}} = \text{diag} \left(\sigma_{\mathbf{x}, \mathbf{x}_{\text{T}}}^2, \sigma_{\mathbf{x}, \mathbf{x}_{\text{T}}}^2, \sigma_{\mathbf{x}, \mathbf{x}_{\phi}}^2 \right)^{-1}$	$\sigma_{\mathbf{x}, \mathbf{x}_{\text{T}}} = 0.05 \text{ m}$ $\sigma_{\mathbf{x}, \mathbf{x}_{\phi}} = 0.01 \text{ rad}$
$\mathbf{P}^{\mathbf{x}, \text{lp}} = \text{diag} \left(\sigma_{\mathbf{x}, \text{lp}_{\phi}}^2, \sigma_{\mathbf{x}, \text{lp}_{\phi}}^2 \right)^{-1}$	$\sigma_{\mathbf{x}, \text{lp}_{\phi}} = 0.5 \text{ m}$ $\sigma_{\mathbf{x}, \text{lp}_{\phi}} = 0.03 \text{ rad}$

B. Evaluation Implementation

The localization performance is evaluated after the selected environment has been traversed multiple times. A separate map is constructed for each evaluation pass that includes all drives except its own one in the landmark finding process. This avoids an unfair evaluation. The following parameters are empirically derived and used in this process: $d_{\text{lp}, \text{thres}} = 0.3 \text{ m}$, $N_{\text{lp}, \text{thres}} = 2$, $d_{\text{l}, \text{ch}, \text{thres}} = 0.09 \text{ m}$, $d_{\text{l}, \text{prj}, \text{thres}} = 1.5 \text{ m}$. For graph optimization, the open source library GTSAM [56] is used. All required factor types have implementations of the error functions shipped with the library, so the following are used: `BetweenFactorPose2`, `BearingRangeFactor2D` and `PriorFactorPoint2`. A `PriorFactorPose2` is introduced in case the number of observed and associated landmarks is insufficient and the global vehicle pose is underconstrained. The prior factor constrains the last pose node within the sliding window with a previously derived pose estimate such that the current estimate is effectively the integration of the odometry factors. For the information matrices of the factors, empirically found uncorrelated standard deviations were chosen. The values can be found in Table IV.

Because each iteration of the localization loop is an incremental update of the pose graph, the `iSAM2` [57] implementation is used, which is efficient for incremental graph optimization by taking advantage of a Bayes tree data structure. In each measurement cycle, the point-shaped landmark observations are queried for map counterparts and found matches are incorporated into the graph. Contrary, line-shaped landmarks are considered only in every 10th frame or when the number of point-shaped matches is less than 5. While this has no negative impact on the localization performance according to the experimental validation, it saves computational time because the line-shaped landmark distance measure calculation is more demanding compared to point-shaped landmarks and an increase of the graph’s node size occurs for each observation (cf. Section III-F). While this work’s focus is not on a highly optimized implementation of the proposed approach, attention is paid to only use algorithms that are able to run in a vehicle from a complexity point of view. The recent trend of increasingly widespread graphics processing units for highly parallel operation in the automotive context is taken into account. All radar signal processing and gridmapping is implemented in CUDA and real-time capable. However, the remaining parts of the building blocks in Fig. 2 are implemented in Python and the evaluation is run offline.

TABLE V
OVERVIEW OF ROUTES USED FOR EVALUATION

Route	Single-Pass Route Length	Evaluated Ride Duration	Environment Type
Frankfurt	7 km	45 min	urban, industrial
Ingolstadt	10 km	75 min	urban, industrial
Ulm	5 km	35 min	village, rural

C. Dataset

The proposed localization framework is evaluated on three different routes in Germany that are part of the cooperative project @CITY. Table V gives an overview over the different routes. Three passes per route are selected for evaluation. While the metric route length refers to one pass, the evaluation duration includes all three passes. Each route was driven in the same direction for every pass to eliminate any possible influence on the study’s main objective. The dataset is chosen to include diverse scenarios, ranging from rural sections, over populated areas of different density, to industrial parks. An example traversal of the Ulm route is shown in Fig. 10 with an amplitude-only PreCFAR map based on the ground truth trajectory and landmark positions of some sections. Moreover, a comparison of radar map and HD map is shown.

D. Localization Accuracy

The quantitative evaluation of the localization result is based on absolute trajectory errors. Assuming that post-processed GNSS/IMU data provides a ground truth pose \mathbf{x}_{gt} , the error to the estimated pose $\hat{\mathbf{x}}$ is calculated. Let a pose \mathbf{x} be expressed as a pair of rotation $\mathbf{R} \in \text{SO}(2)$ and translation $\mathbf{t} \in \mathbb{R}^2$. Then, the absolute trajectory errors of interest are

- $\epsilon_{\text{t}} = (\epsilon_{\text{long}} \ \epsilon_{\text{lat}})^T = \mathbf{R}_{\text{gt}}^{-1} (\hat{\mathbf{t}} - \mathbf{t}_{\text{gt}})$ for a translational and
- $\epsilon_{\text{rot}} = \arccos \left(0.5 \text{tr} \left(\mathbf{R}_{\text{gt}}^{-1} \hat{\mathbf{R}} \right) \right)$ for a rotational part.

For better interpretation, the translational part is assessed by its components in longitudinal and lateral directions ϵ_{long} and ϵ_{lat} , respectively. The time series of trajectory errors is reduced to two scalar performance figures for evaluation in the following: maximum and RMSE. In order to avoid any influence from inaccuracies of the ground truth system, results are only included in the performance figure calculation when a carrier phase solution is available (cf. Section IV-A). Moreover, periods when the vehicle comes to a standstill (more specifically $v \leq 0.5 \text{ m s}^{-1}$), e.g. at a traffic light, are not included to avoid skewing the error distribution.

Table VI gives an overview of the results for all drives using fully polarimetric information. The column “Reliable GNSS” indicates how often the precise ground truth solution was available. Comparing the longitudinal and lateral results first, a difference can be observed. In general, the lateral accuracy is better, especially in terms of RMSE. This can be explained by the structure of typical automotive environments. The driving lanes are typically bounded, e.g. by curbstones, guardrails or grass edges. These boundaries are well detectable by radar, so the localization system can orient itself to these objects to derive a good estimate of the lateral position. As can be seen from the maximum lateral trajectory errors, it is sufficient to infer the traveled lane in all evaluated drives.

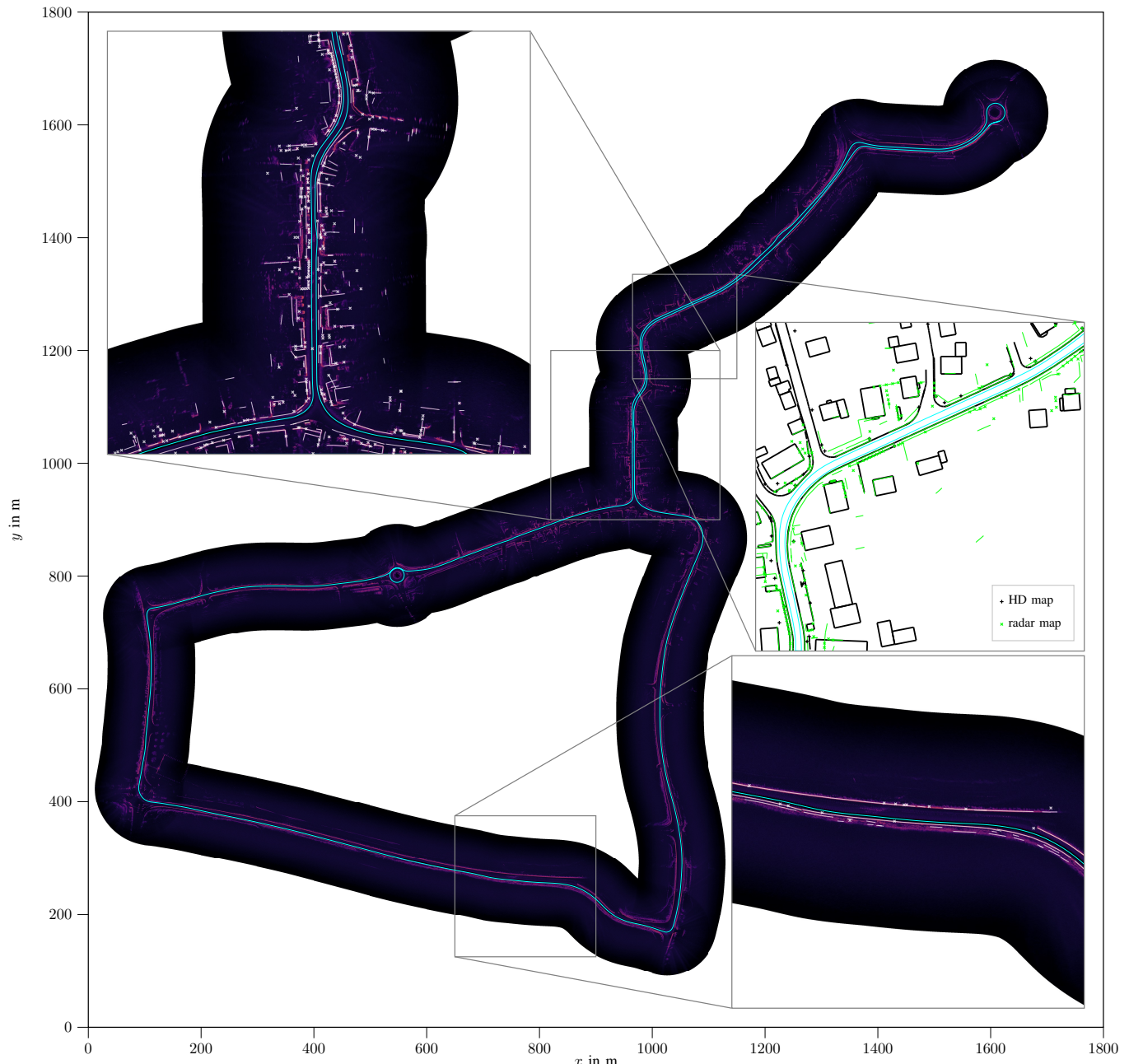


Fig. 10. The Ulm route is shown as an amplitude PreCFAR gridmap. Due to the high resolution, the reader is invited to zoom into the figure. The ground truth trajectory is shown in cyan. Only in the zoomed excerpts, the map landmarks are visualized in white and a significant difference in density can be observed depending on the environment. An additional excerpt allows correlating the generated radar map with a third-party HD map. While a good general spatial agreement can be observed, numerous additional point-shaped landmarks are found in the radar map (mainly fence posts not included in HD map).

TABLE VI
LOCALIZATION ACCURACY USING FULLY POLARIMETRIC INFORMATION

Route	Drive	Reli. GNSS	longitudinal (ϵ_{long})		lateral (ϵ_{lat})		rotational (ϵ_{rot})	
			RMSE	max	RMSE	max	RMSE	max
Frankfurt	#1	76 %	0.12 m	0.84 m	0.06 m	0.45 m	0.44°	2.77°
	#2	84 %	0.11 m	0.74 m	0.06 m	0.37 m	0.45°	2.91°
	#3	87 %	0.15 m	1.29 m	0.06 m	0.49 m	0.48°	3.83°
Ingolstadt	#1	91 %	0.08 m	0.36 m	0.05 m	0.29 m	0.39°	2.57°
	#2	93 %	0.09 m	0.34 m	0.05 m	0.39 m	0.41°	2.92°
	#3	92 %	0.08 m	0.37 m	0.05 m	0.38 m	0.37°	2.69°
Ulm	#1	87 %	0.13 m	0.76 m	0.06 m	0.46 m	0.46°	2.67°
	#2	85 %	0.13 m	0.73 m	0.06 m	0.25 m	0.45°	1.81°
	#3	85 %	0.10 m	0.43 m	0.06 m	0.34 m	0.44°	2.30°

Contrary to that, there might not always be enough infrastructure available to allow a localization with comparable accuracy in longitudinal direction. An example of a spatially resolved translational trajectory error in both directions is shown in Fig. 11. In comparison to Fig. 10, a correlation between the areas of low point-shaped landmark density and larger longitudinal trajectory errors can be identified. While the lane boundaries allow for precise lateral localization, the number of landmarks that help in longitudinal direction (point-shaped or orthogonal line-shaped landmarks) is insufficient and the integration error of the ego-motion starts to show. An improvement could be possible by refining the radar-based ego-motion estimation or by adding other sensor modalities.

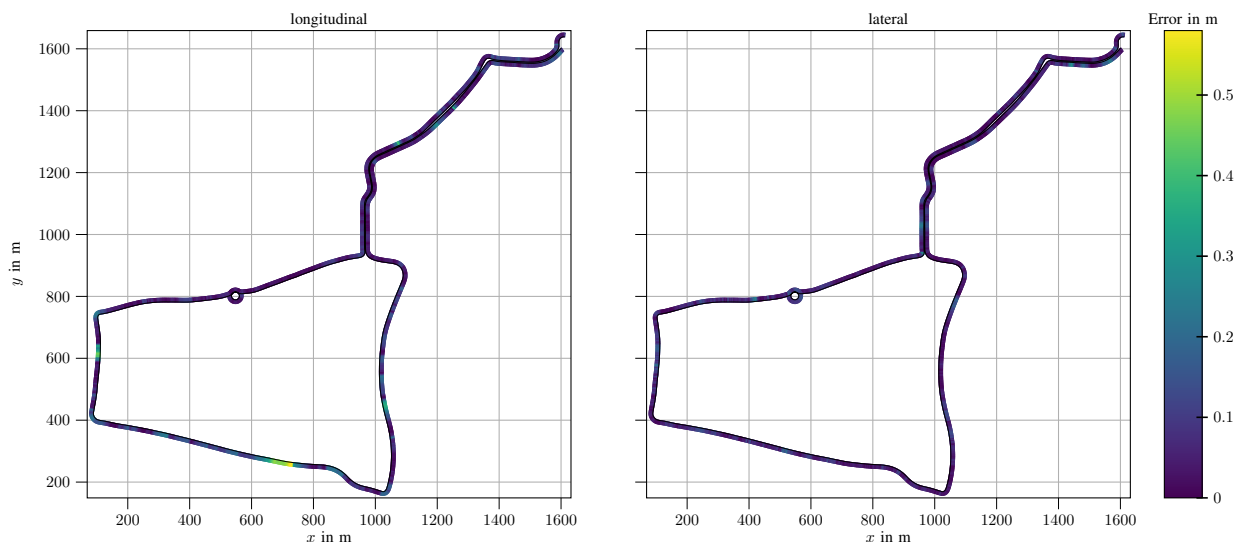


Fig. 11. The spatial distribution of the longitudinal and lateral trajectory errors of drive #3 in Ulm allows identification of areas with increased errors. The generally better performance in the lateral compared to the longitudinal direction can also be observed in this example. By correlating the areas of low point-shaped landmark density depicted in Fig. 10, the cause of larger localization errors can be understood.

However, one can argue that this behavior only shows when the longitudinal position is least critical. As soon as it becomes more critical for potential turns, there is usually more infrastructure available for longitudinal localization. Comparing the results of the routes in different cities among each other, a significantly better result in terms of translational and rotational RMSEs as well as the longitudinal maximum error can be observed for all drives in Ingolstadt. The results' similarity of the three Ingolstadt drives leads to the conclusion that this environment is the easiest one for localization. This is due to the fact that a sufficient amount of localization-suitable infrastructure is available everywhere along this route. The Frankfurt and Ulm routes, on the other hand, have sections where this is not the case, resulting in worse accuracies. As shown by the example in Fig. 11, this occurs on connecting roads, where the low amount of infrastructure (guardrail posts or guide posts) is occluded by low vegetation, so that a robust detection by radar is not ensured.

To assess the impact of the ego-velocity on the localization accuracy, the translational error vector length is plotted over the ego-velocity in Fig. 12. The plotted linear regression does not show a tendency of increased localization errors for higher velocities in Ingolstadt and Frankfurt. In contrast, a small positive correlation is apparent for Ulm. However, speed limits allow higher velocities only in the area of lower landmark density as identified in Fig. 10, such that the apparent correlation is justified otherwise. Consequently, a general degradation with increasing velocities can not be stated.

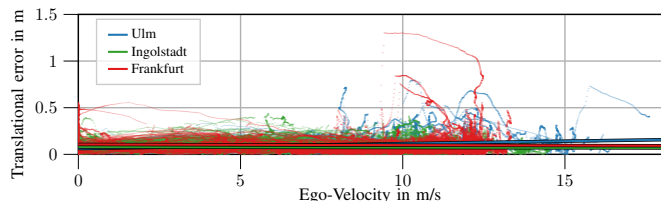


Fig. 12. The distribution of the translational localization error over all three drives per city shows an apparent positive correlation with the ego-velocity for the Ulm route, which is explainable by the landmark density in Fig. 10.

E. Influence of Polarimetric Information

In order to compare the effect of different levels of polarization information on the localization accuracy, the fully polarimetric measurement data was sub-sampled in a number of experiments. While this omitting of some polarization channels to simulate a radar with limited polarimetric information does not preserve the back-scattered power (i.e. a non-polarimetric radar could have more effective illumination time with the same overall measurement duration because no TDM polarization switching is needed), the effect on the localization result is expected to be small. This is assumed because low reflectivity landmark candidates constitute no robust landmarks and thus offer negligible benefit for localization. The much more decisive impact on exploiting lower reflectivity landmarks is coming from leveraging PreCFAR gridmaps to avoid CFAR's masking such that line-shaped candidates constitute a continuous area, which is robustly identifiable by the extractor. An example of the negligible effect of the power loss is given in Section III-C2 by the weak curbstone.

The comparison between the different polarization levels is done via complementary cumulative distribution functions (CCDFs) of the rotational trajectory error and of the translational errors in lateral and longitudinal directions. It is defined as $\bar{F}(\epsilon) = 1 - F(\epsilon)$ with the cumulative distribution function $F(\epsilon)$. $\bar{F}(\epsilon)$ is the probability that the trajectory error will take a value greater than ϵ . By using a logarithmic scaling of the y-axis, it is easier to read the lower probability values for the larger trajectory errors in the lower part of the plots.

Additional to the polarimetric information levels in the circular basis \mathcal{B}_{LR} , which could be derived by omitting elements, the channels of a linear basis \mathcal{B}_{HV} were considered for evaluation. For this, the fully polarimetric covariances in the circular basis were transformed to the linear basis [58] and subsampled from there if necessary. Equation (3) remains valid with the only change that the covariances are now in the linear basis $(\mathbf{C}_{\mathcal{B}_{HV}}, \Sigma_{\mathcal{B}_{HV}})$.

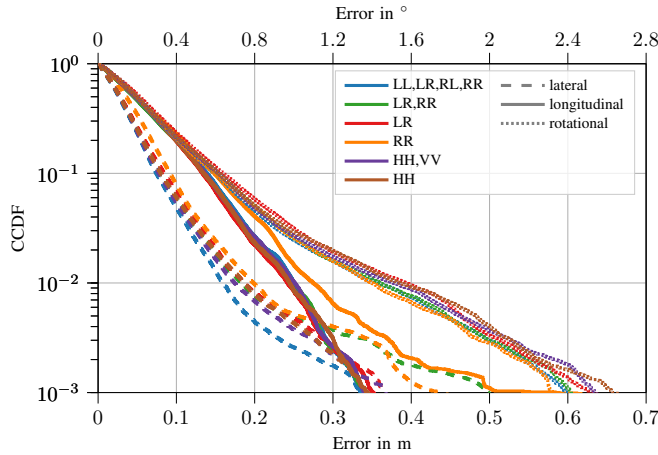


Fig. 13. The distribution of trajectory errors accumulated over all three drives along the Ingolstadt route shows no significant performance difference depending on the polarization level used, except for the single polarization evaluation of the even-bounce channel RR.

For the fully polarimetric case, one can show that the Wishart distance is the same irrespective of which of the two bases is chosen. Therefore, the linear fully polarimetric case is not shown in the following figures. Dual and single polarimetric configurations in a linear basis are included in a way comparable with the circular basis. Only the single cross-polarized case (HV or VH) is dropped because of significantly worse results, which would have made unfavorable rescaling of the figures necessary. This result is expected as even-bounce scattering with the specific orientation required for a response in these channels is rarely occurring at suitable landmarks.

Due to the covariance formulation in Eq. (2), the absolute phase is neglected in the single polarimetric experiments (LR or RR or HH) such that only real amplitudes are used. Starting from two polarimetric channels, the two-dimensional complex covariance is spanned and the relative phases between channels are included additionally to the amplitudes by the off-diagonal elements representing a part of the scattering characteristic.

In Fig. 13, the joint distribution over all three drives along the Ingolstadt route is shown. Confirming the previous observation of favorable results on this route, there is generally no significant degradation of localization performance even with decreasing polarimetric information content. This supports the hypothesis that a sufficient amount of infrastructure is available and can already be detected by amplitude only. Landmarks that require polarimetric information for reliable detection are not needed due to the abundant presence of other landmarks. A minor exception is observed for the even-bounce single polarization channel RR, which shows worse errors in both translational dimensions. This is not surprising, because a large part of the landmarks in automotive environments exhibit odd-bounce scattering behavior, which makes a localization system relying only on even-bounce scatterers the least preferred realization for such applications.

Different results are found for the more challenging environment on the Ulm routes, as is shown in Fig. 14. Starting with the single even-bounce channel RR, low errors are observed in longitudinal direction compared to the other configurations on this route. This can be explained

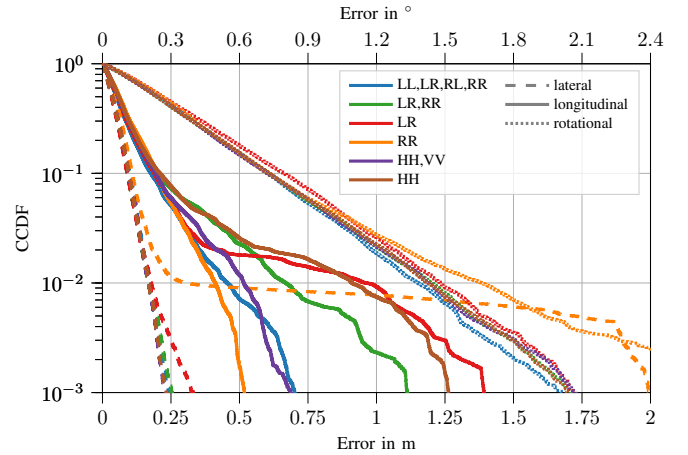


Fig. 14. The distribution of trajectory errors accumulated over all three drives along the Ulm route shows a significant performance difference depending on the employed polarization level.

by the fact that the low occurrence of landmarks with such scattering does not lead to challenges with an unambiguous association. However, especially line-shaped landmarks are rarely even-bounce scatterers that would have helped with the lateral and rotational errors. Accordingly, the results are particularly poor in these dimensions and this polarization configuration is the overall worst case. For the remaining configurations, no remarkable difference in the lateral and rotational errors is observed. A sufficient number of line-shaped landmarks that are extracted by amplitude alone is the reason for this observation. This supports the hypothesis that received power, which is most relevant for extraction of continuous line-shaped landmarks, is not a limiting factor for localization applications. Consequently, the approach of omitting channels can be considered valid. Excluding RR, the longitudinal localization error decreases with an increasing amount of polarimetric information. Contrary to the Ingolstadt route, there is no longer an abundance of robust landmark extractions irrespective of the polarimetric configuration used. The addition of scattering uniqueness as a criterion during landmark extraction seems to offer the expected advantage in this environment. Further evidence that the advantage is not just caused by the ability to receive power from even- and odd-bounce objects can be derived by considering the linear basis results. With the HH configuration, even- and odd-bounce scattering of most relevant objects (excluding rarely occurring 45° rotated dihedral structures) is received but the performance is still comparable to the inferior LR result. Only the linear dual polarimetric configuration HH,VV shows a significant improvement. Although no reception of other polarizations is added, the ability of a scattering-based extraction by distinguishing between even- and odd-bounce scattering instead of a purely amplitude-based approach enables the improvement.

V. CONCLUSION

This paper presented a radar-only landmark-based localization approach that exploits polarimetric scattering information for a more robust detection of landmarks. Extensive real-world experiments with more than 2.5 h of driving demonstrated the high accuracy of the localization in diverse environments.

When using fully polarimetric data, average RMS errors of 0.11 m, 0.06 m and 0.43° are observed for longitudinal, lateral and rotational components, respectively. It was also shown how the localization performance benefits from adding increasing amounts of polarimetric information in challenging scenarios. A limitation of the approach is that the map construction relies on the availability of a ground truth pose. Therefore, future work involves constructing the maps at least partially in a SLAM fashion when no ground truth is available, and studying how this affects the localization performance.

REFERENCES

- [1] Y. Lu, H. Ma, E. Smart, and H. Yu, "Real-time performance-focused localization techniques for autonomous vehicle: A review," *IEEE Transactions on Intelligent Transportation Systems*, vol. 23, no. 7, pp. 6082–6100, 2022.
- [2] M. Bijelic, T. Gruber, F. Mannan, F. Kraus, W. Ritter, K. Dietmayer, and F. Heide, "Seeing through fog without seeing fog: Deep multimodal sensor fusion in unseen adverse weather," in *Proceedings of the IEEE/CVF Conference on Computer Vision and Pattern Recognition (CVPR)*, 2020.
- [3] M. Holder, S. Hellwig, and H. Winner, "Real-time pose graph SLAM based on radar," in *2019 IEEE Intelligent Vehicles Symposium (IV)*, 2019, pp. 1145–1151.
- [4] K. Werber, J. Klappstein, J. Dickmann, and C. Waldschmidt, "Interesting areas in radar gridmaps for vehicle self-localization," in *2016 IEEE MTT-S International Conference on Microwaves for Intelligent Mobility (ICMIM)*, 2016, pp. 1–4.
- [5] J.-S. Lee and E. Pottier, *Polarimetric radar imaging: from basics to applications*. CRC press, 2017.
- [6] H. Iqbal, F. Bögelsack, and C. Waldschmidt, "Polarimetric RCS analysis of traffic objects," in *2017 European Radar Conference (EURAD)*, 2017, pp. 49–52.
- [7] F. Weishaupt, A. Uzair, R. Moch, H.-L. Bloecher, J. F. Tilly, J. Dickmann, and D. Heberling, "Polarimetric scattering mechanism analysis of automotive landmarks," in *2020 21st International Radar Symposium (IRS)*, 2020, pp. 379–384.
- [8] F. Weishaupt, J. F. Tilly, J. Dickmann, and D. Heberling, "Polarimetric covariance gridmaps for automotive self-localization," in *2020 IEEE 23rd International Conference on Information Fusion (FUSION)*, 2020, pp. 1–8.
- [9] Z. Hong, Y. Petillot, and S. Wang, "RadarSLAM: Radar based large-scale SLAM in all weathers," in *2020 IEEE/RSJ International Conference on Intelligent Robots and Systems (IROS)*, 2020, pp. 5164–5170.
- [10] Ş. Säfteşcu, M. Gadd, D. De Martini, D. Barnes, and P. Newman, "Kidnapped radar: Topological radar localisation using rotationally-invariant metric learning," in *2020 IEEE International Conference on Robotics and Automation (ICRA)*, 2020, pp. 4358–4364.
- [11] W. Wang, P. P. B. de Gusmão, B. Yang, A. Markham, and N. Trigoni, "Radarloc: Learning to relocalize in FMCW radar," in *2021 IEEE International Conference on Robotics and Automation (ICRA)*, 2021, pp. 5809–5815.
- [12] D. Barnes, M. Gadd, P. Murcutt, P. Newman, and I. Posner, "The oxford radar robotcar dataset: A radar extension to the oxford robotcar dataset," in *2020 IEEE International Conference on Robotics and Automation (ICRA)*, 2020, pp. 6433–6438.
- [13] G. Kim, Y. S. Park, Y. Cho, J. Jeong, and A. Kim, "Mulran: Multimodal range dataset for urban place recognition," in *2020 IEEE International Conference on Robotics and Automation (ICRA)*, 2020, pp. 6246–6253.
- [14] S. H. Cen and P. Newman, "Precise ego-motion estimation with millimeter-wave radar under diverse and challenging conditions," in *2018 IEEE International Conference on Robotics and Automation (ICRA)*, 2018, pp. 6045–6052.
- [15] —, "Radar-only ego-motion estimation in difficult settings via graph matching," in *2019 IEEE International Conference on Robotics and Automation (ICRA)*, 2019, pp. 298–304.
- [16] D. Barnes and I. Posner, "Under the radar: Learning to predict robust keypoints for odometry estimation and metric localisation in radar," in *2020 IEEE International Conference on Robotics and Automation (ICRA)*, 2020, pp. 9484–9490.
- [17] K. Burnett, D. J. Yoon, A. P. Schoellig, and T. D. Barfoot, "Radar odometry combining probabilistic estimation and unsupervised feature learning," *arXiv preprint arXiv:2105.14152*, 2021.
- [18] D. Kellner, M. Barjenbruch, J. Klappstein, J. Dickmann, and K. Dietmayer, "Instantaneous ego-motion estimation using multiple doppler radars," in *2014 IEEE International Conference on Robotics and Automation (ICRA)*, 2014, pp. 1592–1597.
- [19] S. Clark and H. Durrant-Whyte, "Autonomous land vehicle navigation using millimeter wave radar," in *1998 IEEE International Conference on Robotics and Automation (ICRA)*, vol. 4, 1998, pp. 3697–3702.
- [20] M. Lundgren, E. Stenborg, L. Svensson, and L. Hammarstrand, "Vehicle self-localization using off-the-shelf sensors and a detailed map," in *2014 IEEE Intelligent Vehicles Symposium Proceedings*, 2014, pp. 522–528.
- [21] M. Rapp, M. Hahn, M. Thom, J. Dickmann, and K. Dietmayer, "Semi-markov process based localization using radar in dynamic environments," in *2015 IEEE International Intelligent Transportation Systems Conference (ITSC)*, 2015, pp. 423–429.
- [22] M. Cornick, J. Koechling, B. Stanley, and B. Zhang, "Localizing ground penetrating radar: A step toward robust autonomous ground vehicle localization," *Journal of Field Robotics*, vol. 33, pp. 82–102, 2016.
- [23] F. Schuster, M. Wörner, C. Keller, M. Haueis, and C. Curio, "Robust localization based on radar signal clustering," in *2016 IEEE Intelligent Vehicles Symposium (IV)*, 2016, pp. 839–844.
- [24] E. Ward and J. Folkesson, "Vehicle localization with low cost radar sensors," in *2016 IEEE Intelligent Vehicles Symposium (IV)*, 2016, pp. 864–870.
- [25] K. Yoneda, N. Hashimoto, R. Yanase, M. Aldibaja, and N. Sukanuma, "Vehicle localization using 76GHz omnidirectional millimeter-wave radar for winter automated driving," in *2018 IEEE Intelligent Vehicles Symposium (IV)*, 2018, pp. 971–977.
- [26] M. Li, W. Jia, M. Kunert, R. Henze, and F. Küçükay, "Environment mapping and vehicle localization with a high-resolution radar prototype," in *Proc. 5th Int. Symposium on Future Active Safety Technology toward Zero Accidents*, 2019.
- [27] P. A. Iannucci, L. Narula, and T. E. Humphreys, "Cross-modal localization: Using automotive radar for absolute geolocation within a map produced with visible-light imagery," in *2020 IEEE/ION Position, Location and Navigation Symposium (PLANS)*, 2020, pp. 285–296.
- [28] S. Jürgens, N. Koch, and M.-M. Meinecke, "Radar-based automotive localization using landmarks in a multimodal sensor graph-based approach," in *2020 21st International Radar Symposium (IRS)*, 2020, pp. 373–378.
- [29] L. Narula, P. A. Iannucci, and T. E. Humphreys, "Automotive-radar-based 50-cm urban positioning," in *2020 IEEE/ION Position, Location and Navigation Symposium (PLANS)*, 2020, pp. 856–867.
- [30] T. Ort, I. Gilitschenski, and D. Rus, "Autonomous navigation in inclement weather based on a localizing ground penetrating radar," *IEEE Robotics and Automation Letters*, vol. PP, pp. 1–1, 02 2020.
- [31] A. Pishchvari, M. Stefer, and B. Tibken, "Robust range-doppler registration with hd maps," in *2020 5th International Conference on Control and Robotics Engineering (ICCRE)*, 2020, pp. 140–147.
- [32] H. Yin, Y. Wang, L. Tang, and R. Xiong, "Radar-on-lidar: metric radar localization on prior lidar maps," in *2020 IEEE International Conference on Real-time Computing and Robotics (RCAR)*, 2020, pp. 1–7.
- [33] N. Engel, V. Belagiannis, and K. Dietmayer, "Attention-based vehicle self-localization with hd feature maps," in *2021 IEEE International Intelligent Transportation Systems Conference (ITSC)*, 2021, pp. 76–83.
- [34] B. Otake, "Automotive radar for localization in gnss-denied environments," Master's thesis, KTH Royal Institute of Technology, Stockholm, 2021.
- [35] K. Burnett, Y. Wu, D. J. Yoon, A. P. Schoellig, and T. D. Barfoot, "Are we ready for radar to replace lidar in all-weather mapping and localization?" *IEEE Robotics and Automation Letters*, pp. 1–8, 2022.
- [36] R. Yanase, D. Hirano, M. Aldibaja, K. Yoneda, and N. Sukanuma, "Lidar- and radar-based robust vehicle localization with confidence estimation of matching results," *Sensors*, vol. 22, no. 9, 2022.
- [37] H. Yin, R. Chen, Y. Wang, and R. Xiong, "Rall: End-to-end radar localization on lidar map using differentiable measurement model," *IEEE Transactions on Intelligent Transportation Systems*, vol. 23, no. 7, pp. 6737–6750, 2022.
- [38] P.-C. Kung, C.-C. Wang, and W.-C. Lin, "A normal distribution transform-based radar odometry designed for scanning and automotive radars," in *2021 IEEE International Conference on Robotics and Automation (ICRA)*, 2021, pp. 14417–14423.
- [39] T. Freialdenhoven, T. Bertuch, S. Stanko, D. Nötel, D. I. L. Vorst, and T. Dallmann, "Design of a polarization rotating SIW-based reflector for polarimetric radar application," *IEEE Transactions on Antennas and Propagation*, vol. 68, no. 11, pp. 7414–7422, 2020.
- [40] S. Trummer, G. F. Hamberger, R. Koerber, U. Siart, and T. F. Eibert, "Performance analysis of 79 GHz polarimetric radar sensors for

autonomous driving,” in *2017 European Radar Conference (EuRAD)*, 2017, pp. 41–44.

- [41] T. Visentin, J. Hasch, and T. Zwick, “Polarimetric RCS measurements of selected two-wheeled vehicles for automotive radar,” in *2017 European Radar Conference (EuRAD)*, 2017, pp. 53–56.
- [42] J. F. Tilly, O. Schumann, F. Weishaupt, J. Dickmann, and G. Waniliek, “Polarimetric information representation for radar based road user detection with deep learning,” in *2021 IEEE 24th International Conference on Information Fusion (FUSION)*, 2021, pp. 1–6.
- [43] H. Iqbal, C. Knill, M. Z. Khan, T. Chaloun, and C. Waldschmidt, “Polarimetric SAR for automotive applications,” in *2018 European Radar Conference (EuRAD)*, 2018, pp. 30–33.
- [44] J. M. Merlo and J. A. Nanzer, “A C-band fully polarimetric automotive synthetic aperture radar,” *IEEE Transactions on Vehicular Technology*, vol. 71, no. 3, pp. 2587–2600, 2022.
- [45] S. Clark and G. Dissanayake, “Simultaneous localisation and map building using millimetre wave radar to extract natural features,” in *1999 IEEE International Conference on Robotics and Automation (ICRA)*, May 1999, pp. 1316–1321.
- [46] F. Weishaupt, K. Werber, J. Tilly, J. Dickmann, and D. Heberling, “Polarimetric radar for automotive self-localization,” in *2019 20th International Radar Symposium (IRS)*, 2019, pp. 1–8.
- [47] F. Weishaupt, P. S. Will, N. Appenrodt, J. F. Tilly, J. Dickmann, and D. Heberling, “Robust point-shaped landmark detection using polarimetric radar,” in *2021 IEEE Intelligent Vehicles Symposium (IV)*, 2021, pp. 859–865.
- [48] F. Weishaupt, N. Appenrodt, J. F. Tilly, J. Dickmann, and D. Heberling, “PreCFAR gridmaps for automotive radar,” in *2021 European Radar Conference (EuRAD)*, 2022, pp. 161–164.
- [49] F. Weishaupt, J. F. Tilly, N. Appenrodt, J. Dickmann, and D. Heberling, “Calibration and signal processing of polarimetric radar data in automotive applications,” in *2022 Microwave Mediterranean Symposium (MMS)*, 2022, pp. 1–6.
- [50] K. Werber, M. Rapp, J. Klappstein, M. Hahn, J. Dickmann, K. Dietmayer, and C. Waldschmidt, “Automotive radar gridmap representations,” in *2015 IEEE MTT-S International Conference on Microwaves for Intelligent Mobility (ICMIM)*, 2015, pp. 1–4.
- [51] J.-S. Lee, M. R. Grunes, and R. Kwok, “Classification of multi-look polarimetric SAR imagery based on complex Wishart distribution,” *International Journal of Remote Sensing*, vol. 15, no. 11, 1994.
- [52] J. L. Bentley, “Multidimensional binary search trees used for associative searching,” *Commun. ACM*, vol. 18, no. 9, p. 509–517, sep 1975.
- [53] K. Werber, J. Klappstein, J. Dickmann, and C. Waldschmidt, “Association of straight radar landmarks for vehicle self-localization,” in *2019 IEEE Intelligent Vehicles Symposium (IV)*, 2019, pp. 736–743.
- [54] U. Ramer, “An iterative procedure for the polygonal approximation of plane curves,” *Computer Graphics and Image Processing*, pp. 244–256, 1972.
- [55] Daniel Wilbers, “Graph-based sliding window localization and map refinement for automated vehicles,” Ph.D. dissertation, Rheinische Friedrich-Wilhelms-Universität Bonn, October 2021.
- [56] F. Dellaert and GTSAM-Contributors, “borglab/gtsam - Georgia Tech Smoothing and Mapping Library,” May 2022.
- [57] M. Kaess, H. Johannsson, R. Roberts, V. Ila, J. Leonard, and F. Dellaert, “iSAM2: Incremental smoothing and mapping with fluid relinearization and incremental variable reordering,” in *2011 IEEE International Conference on Robotics and Automation (ICRA)*, 2011, pp. 3281–3288.
- [58] D. G. Michelson, I. G. Cumming, and C. E. Livingstone, “Symmetry properties of the circular polarization covariance matrix,” *Journal of Electromagnetic Waves and Applications*, vol. 11, pp. 719–738, 1997.

Fabio Weishaupt received his B.Sc. and M.Sc. degrees in electrical engineering from RWTH Aachen University, Aachen, Germany, in 2015 and 2017, respectively. His master thesis was carried out at Fraunhofer FHR, Wachtberg, Germany, on vital sign measurements with mmWave radar. Since 2018, he is working towards a Ph.D. degree on the topic of polarimetric radar for automotive self-localization at the research and development department of Mercedes-Benz AG together with RWTH Aachen University, Aachen, Germany. His research interests

include mmWave system design, polarimetry, radar signal processing and perception algorithms.



Julius F. Tilly received his master’s degree in Physics from Technical University of Dortmund in 2017. In his master’s thesis he used Nuclear Magnetic Resonance spectroscopy to investigate ion dynamics in lithium borate glass and sodium ion conductors. Since 2018, he is a PhD student at Mercedes-Benz AG in the research and development department for environment perception. He is researching in the field of road user classification and tracking with radars for autonomous driving. His research interests include polarimetric radars, radar

signal processing and algorithms for environment perception with radars.



Nils Appenrodt received his Dipl.-Ing. degree in electrical engineering from University Duisburg, Germany, in 1996. He was a research assistant in the field of imaging radar systems with University Duisburg. Since 2000, he has been with the group research and advanced engineering, formerly Daimler AG now Mercedes-Benz AG, as a research engineer and manager, where he is working in the field of environment perception systems. His research interests include radar sensor processing, sensor data fusion, advanced driver assistance and autonomous driving

systems.



Pascal Fischer received his B.Sc. and M.Sc. degrees in computer science with specialization in artificial intelligence from Goethe University, Frankfurt am Main, Germany in 2020 and 2021, respectively. His master thesis was carried out at Mercedes-Benz AG, Stuttgart, Germany, on automotive self-localization with polarimetric radar. Since the end of 2021, he is working as a machine learning engineering consultant at Accenture in various industries.



Jürgen Dickmann received the Diploma degree in electrical engineering from University Duisburg, Duisburg, Germany, in 1984. He received the Dr.-Ing. degree from Rheinisch Westfaelische Technische Hochschule Aachen (RWTH), Aachen, Germany. He is the Head of radar sensors and radar-based perception at autonomous driving, Mercedes-Benz AG. In this role, he is responsible for research to serial development of radar and radar-based environmental understanding for autonomous driving for all platforms inside Mercedes-Benz AG. Among

others, he held manager positions at Daimler AG in laser-scanner, sensor-fusion, and situation analysis. He conducted radar developments for radar-based precrash and driver assistant systems for all platforms (passenger cars, busses, van, truck) inside Daimler AG, including E/S-Class. In 1986, he started his career at AEG Research Center, where he did research on III/V-semiconductor processing techniques, mm-Wave device, and MMIC-design (up to 120 GHz) and fabrication.

Dirk Heberling [M’03, SM’10] received his doctoral degree (Dr.-Ing.) in 1993. In 1993, he joined IMST GmbH, Kamp-Lintfort, Germany, to establish a new antenna section, and from 1995 to 2003, he was the head of the Antennas Department. He has been a member of the European Competence Projects for Antennas COST 260, COST 284, IC0603, and IC1102. From 2003 to 2008, he took over the Department of Information and Communication Systems of IMST GmbH, and in 2008, he moved to RWTH Aachen, where he is the head of

the institute and chair for High Frequency Technology. He is a member of VDE and is the German delegate to IC1102. He is a member of the Steering Committee and Organizing Committee for the European Conference on Antennas and Propagation. In 2016, he became the head of the Fraunhofer Institute for High Frequency Physics and Radar Techniques FHR.

